

# Advanced Elastic/Inelastic Nuclear Data Development Project

---

## Fuel Cycle

**Dr. Frank Harmon**

Idaho State University

### In collaboration with:

University of Massachusetts, Lowell

Colorado School of Mines

University of Dallas

Idaho National Laboratory

Los Alamos National Laboratory

University of Kentucky

University of Utah

Texas A&M University

United States Naval Academy

Dan Vega, Federal POC

Bob Hill, Technical POC

# I. Nuclear Theory

## 1) The Optical Model

The optical model is used to analyze the elastic and inelastic scattering of nucleons, deuterons, hellions, tritons, and alpha particles by the nuclei. Since this paper covers primarily neutron-nucleus scattering, the focus will be limited to only that interaction. For the sake of this model, the nucleus is described as a blob of nuclear matter with properties based upon its number of nucleons. This infers that a single potential can describe the interaction of particles with different energies with different nuclei.

A square well potential was initially used to analyze the optical model. This proved to be too inaccurate, however, as the potential is supposed to fall off exponentially at large distances. This can be represented by the Saxon-Woods form factor

$$f(r) = \frac{1}{1 + e^{\frac{r-R}{a}}} \quad (1.1.1)$$

where  $R$  is the radius parameter, and  $a$  is the surface diffuseness parameter. It is useful to define the radius parameter as

$$R = r_o A^{\frac{1}{3}} \quad (1.1.2)$$

where  $r_o$  is a predefined constant which may have a dependence on  $A$ , and  $A$  is the number of nucleons in the nucleus.

The potential can be written generally as

$$V(\mathbf{r}) = V_R(\mathbf{r}) + V_I(\mathbf{r}) + V_S(\mathbf{r}) \quad (1.1.3)$$

where  $V(\mathbf{r})$  is the potential,  $V_R(\mathbf{r})$  is the radial potential independent of spin and isospins,  $V_I(\mathbf{r})$  is the isospin term and  $V_S(\mathbf{r})$  is the spin-orbit term. These terms are defined as

$$\rho_m(\mathbf{r}) = \rho_n(\mathbf{r}) + \rho_p(\mathbf{r}) \quad (1.1.4)$$

where  $\rho_i(\mathbf{r})$  is the charge density of term  $i$  which is either the material  $m$ , protons  $p$  or neutrons  $n$ . From here, the potential terms can be defined as

$$V_R(\mathbf{r}) = \int \rho_m(\mathbf{r}') v_D(|\mathbf{r} - \mathbf{r}'|) d\mathbf{r}' \quad (1.1.5)$$

$$V_I(\mathbf{r}) = \tau_z \int (\rho_p(\mathbf{r}') - \rho_n(\mathbf{r}')) v_\tau(|\mathbf{r} - \mathbf{r}'|) d\mathbf{r}' \quad (1.1.6)$$

while  $V_S(\mathbf{r})$  is complicated and beyond the scope of this paper.

There are certain cases for which the  $V_S(\mathbf{r})$  term can be written out. For elastic scattering of nucleons, the term can be written as

$$V_S(\mathbf{r}) = \left( \frac{\hbar}{m_\pi c} \right)^2 \frac{V_s}{r} \frac{df_3(r)}{dr} \mathbf{L} \cdot \boldsymbol{\sigma} \quad (1.1.7)$$

which leads to the total potential term (after some algebra) to be

$$V(r) = Vf_1(r) + i(W_V f_2(r) + W_S g(r)) + \left( \frac{\hbar}{m_\pi c} \right)^2 \frac{V_s}{r} \frac{df_3(r)}{dr} \mathbf{L} \cdot \boldsymbol{\sigma} \quad (1.1.8)$$

where  $f_i(r)$  is the Saxon-Woods form factors, which may have different radius and diffuseness parameters,  $g(r)$  is the surface-peaked form factor (normally the radial derivative of a Saxon-Woods form factor), and  $W_V$  and  $W_S$  are the volume and surface absorption potentials, respectively.<sup>1</sup> The potential above does not include any spin or magnetic moment term of the target nucleus, but these terms are small in comparison, and can be ignored.

Experiments were run by Glasgow and Foster using a potential similar to the one shown above for neutrons over the energy range of 3 to 15 MeV. The results were found to differ by less than 3% from experimental values for 46 spherical or soft nuclei and by about 20% for hard deformed nuclei. Inelastic scattering can also be shown if there are multiple channels analyzed together. If the wavefunctions of the channels are strongly coupled, this can be shown to represent inelastic scattering.

There are some disadvantages to this model, however. In general, the potentials are over parameterized, such that several different potentials can give equally good fits to experimental data, especially at low energies. Also, the optical model does not account for the creation of a compound nucleus, which must be dealt with before analysis with the optical model. Therefore, the optical model is mostly used to analyze higher-energy interactions that do not have a compound nucleus associated with them.

## 2) The Hauser-Feshbach statistical model

A second scattering theory of note is the Hauser-Feshbach statistical model. It was derived intentionally with inelastic neutron scattering in mind, but it can easily be expanded to elastic scattering and with other nucleons besides neutrons. It is based on the association between the inlet and outlet channels and the theory of Bohr's compound nucleus principles.<sup>2</sup>

The beginnings of this model come from the theory of a compound nucleus. The creation of this compound nucleus leads to a more complicated method of calculating cross sections. This was first discussed by Hauser and Feshbach who derived the following formula

$$\sigma(E|E') = \pi \tilde{\chi}^2 \frac{(\sum_l (2l+1) T_l(E)) (\sum_{l'} (2l'+1) T_{l'}(E')) D_{R^{-1}}(E-E')}{\sum_{l''} (2l''+1) \int_0^E T_{l''}(E'') D_{R^{-1}}(E-E'') dE''}$$

where  $\sigma(E|E')$  is the cross section from energy  $E$  to  $E'$ ,  $\lambda$  is the reduced wavelength of the incident channel,  $T_i(E)$  is the transmission coefficient for that respective energy channel and  $D_{R-1}$  is the inverse of the difference between levels in the residual nucleus.<sup>2</sup>

This model can be re-written in a form that easier to understand. The purpose of this is so that the physics behind the model can be more easily seen. To start, the expression above can be rearranged and solved for one resonance called the Breit-Wigner single resonance formula.<sup>3</sup> This is shown below

$$\sigma_{ab} = \pi\lambda^2 \frac{\Gamma_a^s \Gamma_b^s}{(E - E_s)^2 + \left(\frac{1}{2}\Gamma^s\right)^2} \quad (1.2.1)$$

where  $\Gamma_i^s$  is the partial width of resonance level number  $s$  for decay through channel  $i$ ,  $E$  is the energy of the compound nucleus,  $E_s$  is the resonance energy of the resonance level number  $s$  and  $\Gamma^s$  is the total width of resonance level number  $s$ . If this is summed over all resonances, the Hauser-Feshbach formula arises.<sup>4</sup> This is shown below

$$\sigma_{ab}^{HF}(E) = \pi\lambda^2 \sum_J \omega_a^J \frac{T_a T_b}{\sum_c T_c} W_{ab} \quad (1.2.2)$$

where  $\omega_a^J$  is a statistical factor,  $J$  is the angular momentum of the nucleon,  $\sum_c T_c$  represents the sum of all the transmission coefficients through all possible channels, and  $W_{ab}$  is the width fluctuation factor. The equation for the statistical factor is shown below

$$\omega_a^J = \frac{2J + 1}{(2i_a + 1)(2I_a + 1)} \quad (1.2.3)$$

where  $i_a$  is the projectile spin and  $I_a$  is the target spin.

The formula shown in Eq. (10) is a simplified expression, as it leaves out important details of angular momentum coupling and parity conservation. However, this is usually seen as acceptable enough when dealing with nuclear engineering scattering computations.

The width fluctuation factor can be regarded as the correlation between the incident and outgoing channels. Mainly, if there is no correlation between the two, then  $W_{ab}$  is equal to 1. If there is a correlation, it is less than 1. The fluctuation factor is found experimentally or by numerically solving the Schrödinger Equation for the particular system. The transmission coefficient can be found several different ways, ranging from quantum mechanical S matrix theory or the use of other models (as explained below).<sup>3</sup>

### 3) Uses in Nuclear Data files and MCNP

Several nuclear data files utilize these models in their analysis. This paper will specifically focus on the ENDF and JENDL libraries. The ways that these and other libraries are utilized in MCNP is also discussed.

The ENDF library currently utilizes both the optical and Hauser-Feshbach model.<sup>5</sup> The optical model was used for higher energy evaluations from 10 keV to 30 MeV. It is also used to calculate the transmission

coefficients needed for the Hauser-Feshbach model as well as to fill in gaps that experimental data leaves out.<sup>6</sup> The Hauser-Feshbach model is used in the GNASH-FKK computational code that was used to create some of the ENDF data files.

The JENDL library currently uses the optical model but not the Hauser-Feshbach model.<sup>7</sup> The optical model is used to both as a way to fill in gaps that experimental data leaves out and to describe the shape of the nucleus when calculating capture cross sections. The Hauser-Feshbach model was used in JENDL-3.2, but was excluded in JENDL-3.3. The reasoning behind this was because in JENDL-3.2, capture cross sections at high energies (in the MeV range) were small when calculated with the Hauser-Feshbach model. Recent experiments have shown, however, that the cross section is in the order of milli-barns, which is much higher than previous Hauser-Feshbach calculations.

MCNP uses the ENDF data library almost exclusively.<sup>8</sup> The MCNP package comes with both ENDF/B-VI.6 and ENDF/B-VII.0. The purpose of including the ENDF/B-VI.6 library was to run quality assurance tests. One of the main benefits of the ENDF/B-VII.0 library utilized by MCNP is that a basic temperature dependence given. The original data files were thermally expanded to 293.6K, 600K, 900K, 1200K and 2500K and then processed into ACE format using NJOY99 Version 248. This also means that these files can be thermally expanded using MAKXSF more accurately than the ENDF/B-VI.6 files because there are baselines to expand from.

#### 4) Temperature Evaluations

For a first test, the <sup>56</sup>Fe ENDF/B-VII.0 file is analyzed and modified to show how important the temperature of a nuclide is to the cross section. The basic theory behind the temperature modification has to do with Doppler Broadening. A simple way to look at the method behind Doppler Broadening is shown below

$$\frac{\sigma_1}{\sigma_2} = \sqrt{\frac{T_2}{T_1}} \quad (1.4.1)$$

where  $\sigma_1$  is the cross section in [b] and  $T_1$  is the temperature in [K]. Using the MAKXSF subroutine in MCNP, I thermally expanded the <sup>56</sup>Fe data file to several different temperatures. These plots can be found on the following pages.

Even though these don't appear to be large changes, there are clearly differences in the thermal region that warrant attention. Basically, as the temperature increases, the thermal cross section increases as well. It also shows that the peaks of the resonances (both minimums and maximums) become less pronounced and tend to level towards the middle of the resonance region.

This is of importance when considering which temperature to use when running an MCNP input deck. MCNP cannot update the temperature of the fuel over the lifetime of the reactor, so the cross sections are a constant over all temperatures. This can lead to varying answers in even the most simple results, as will be shown in the next section.

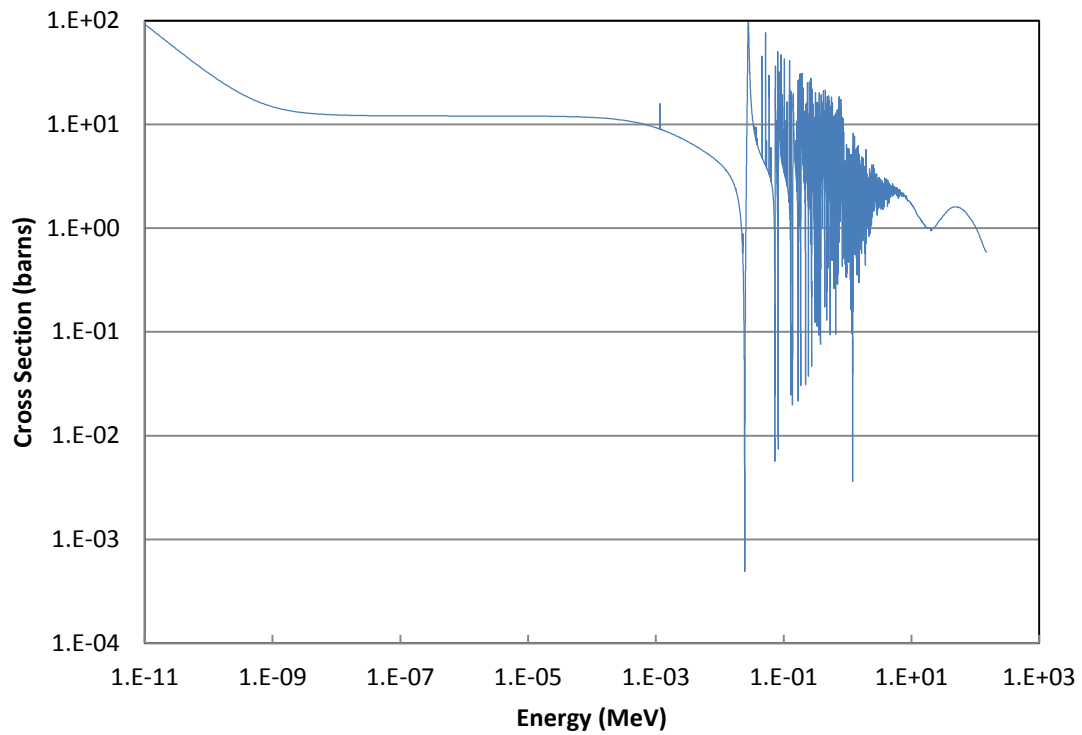


Figure I-1 Total Cross Section of  $^{56}\text{Fe}$  at 294K

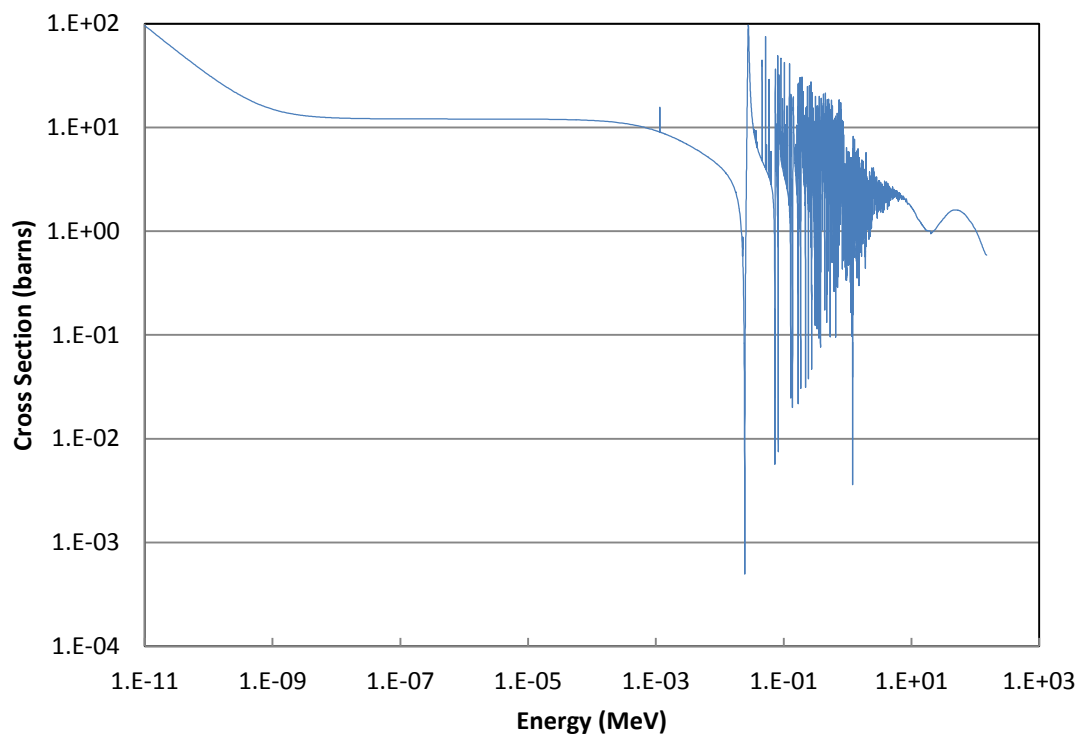


Figure I-2 Total Cross Section of  $^{56}\text{Fe}$  at 314

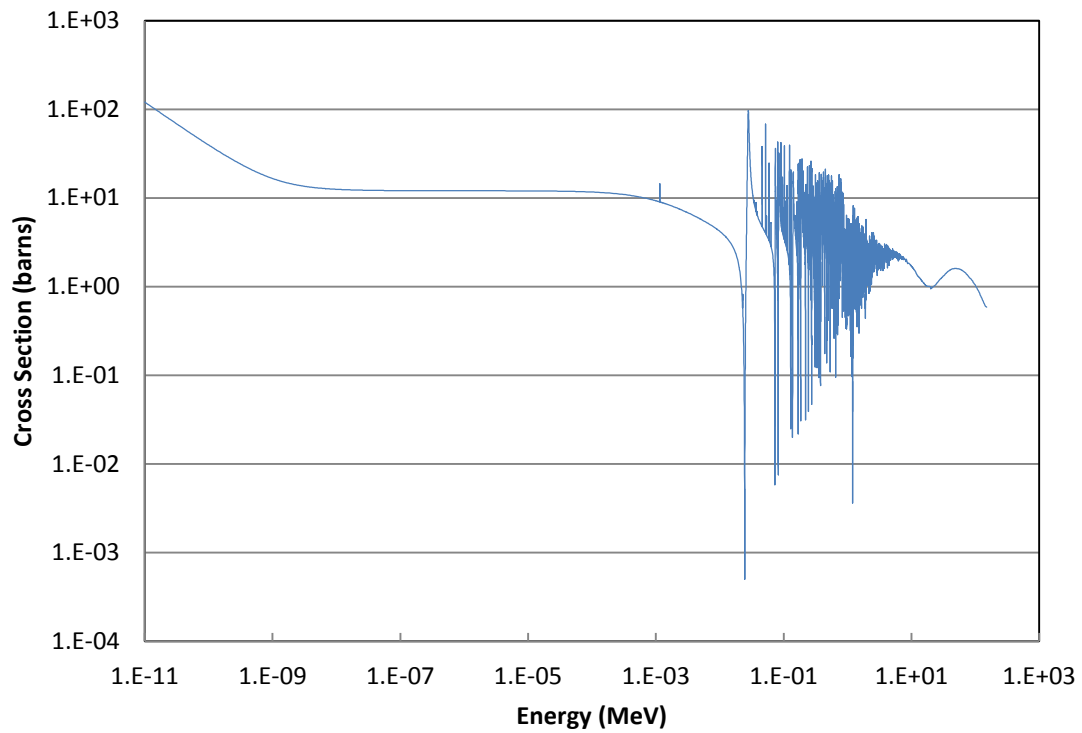


Figure I-3 Total Cross Section of  $^{56}\text{Fe}$  at 500K

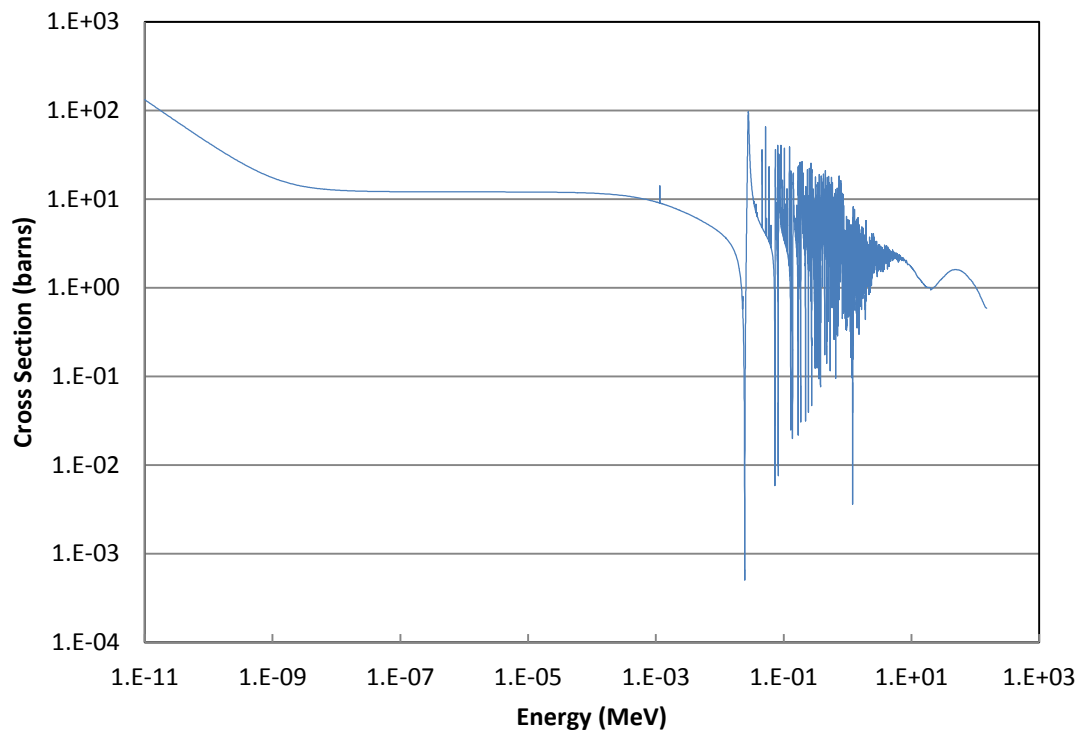


Figure I-4 Total Cross Section of  $^{56}\text{Fe}$  at 600K

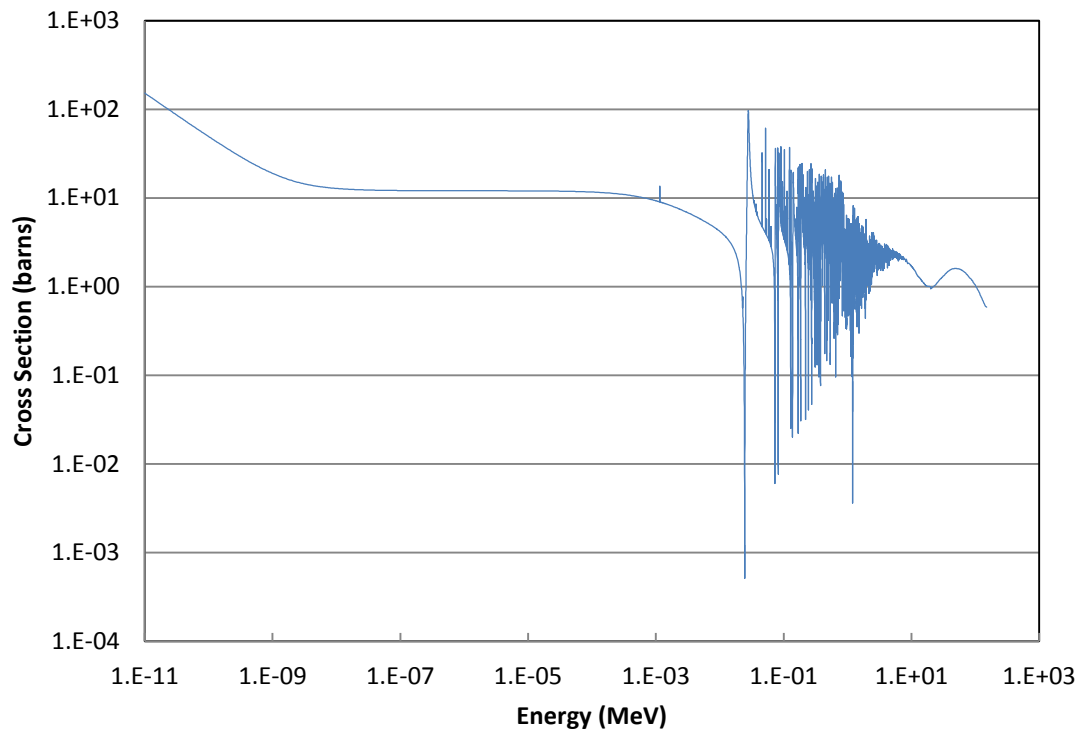


Figure I-5 Total Cross Section of  $^{56}\text{Fe}$  at 800K

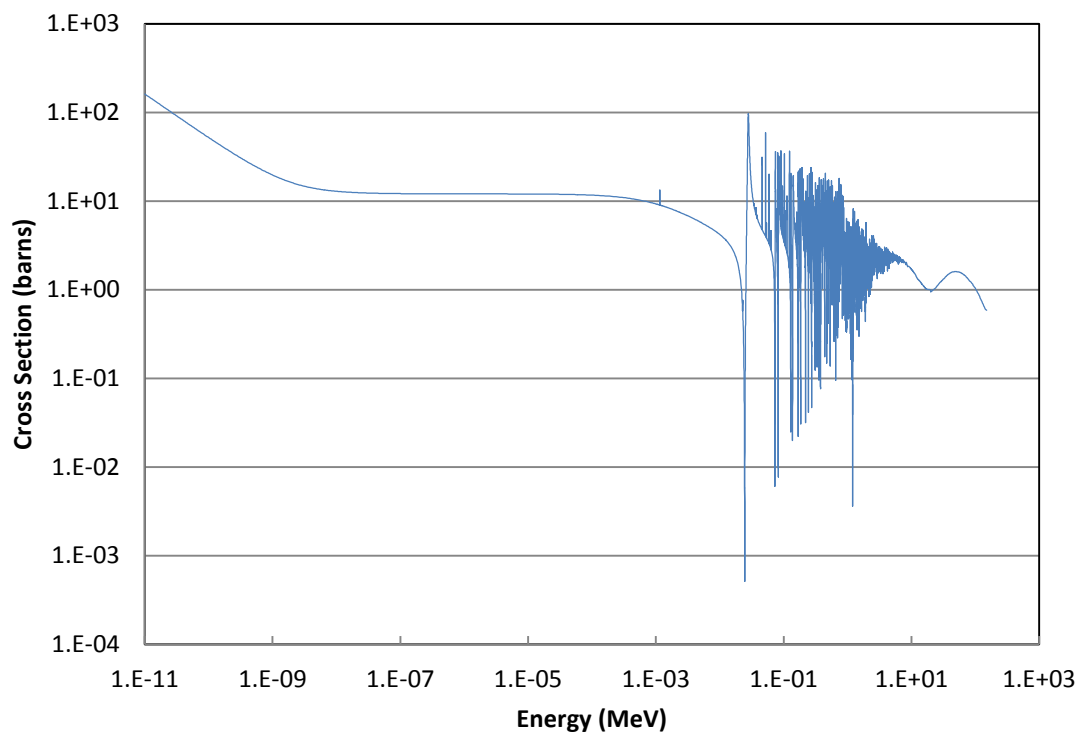


Figure I-6 Total Cross Section of  $^{56}\text{Fe}$  at 900K



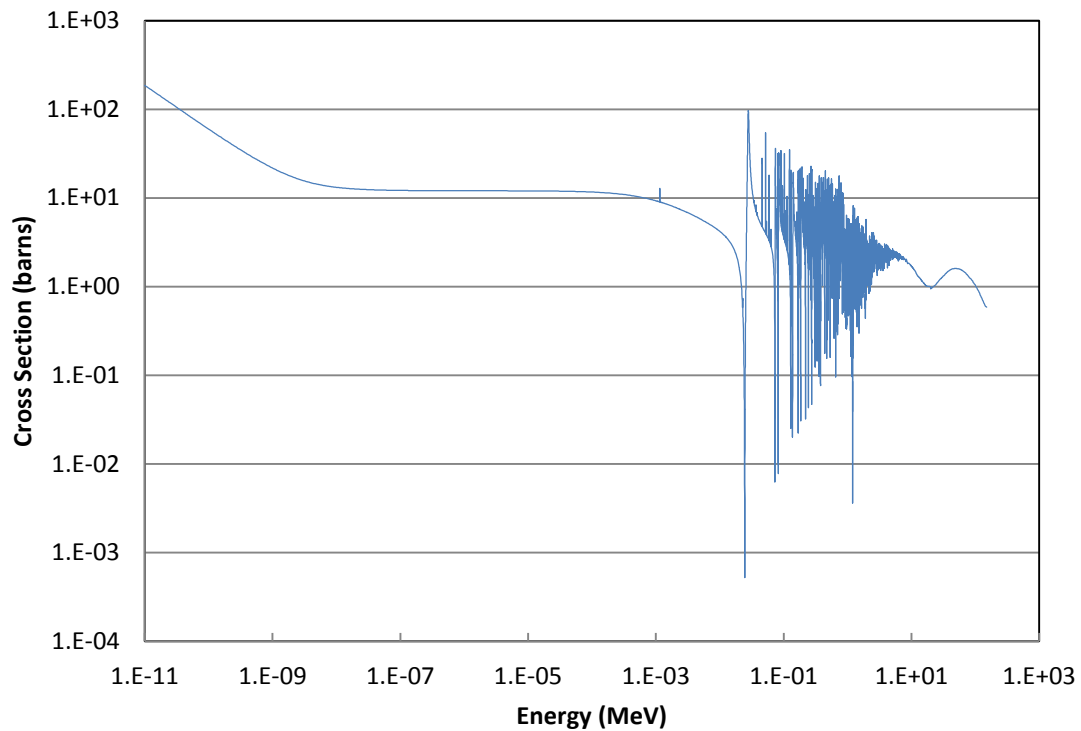


Figure I-7 Total Cross Section of  $^{56}\text{Fe}$  at 1200K

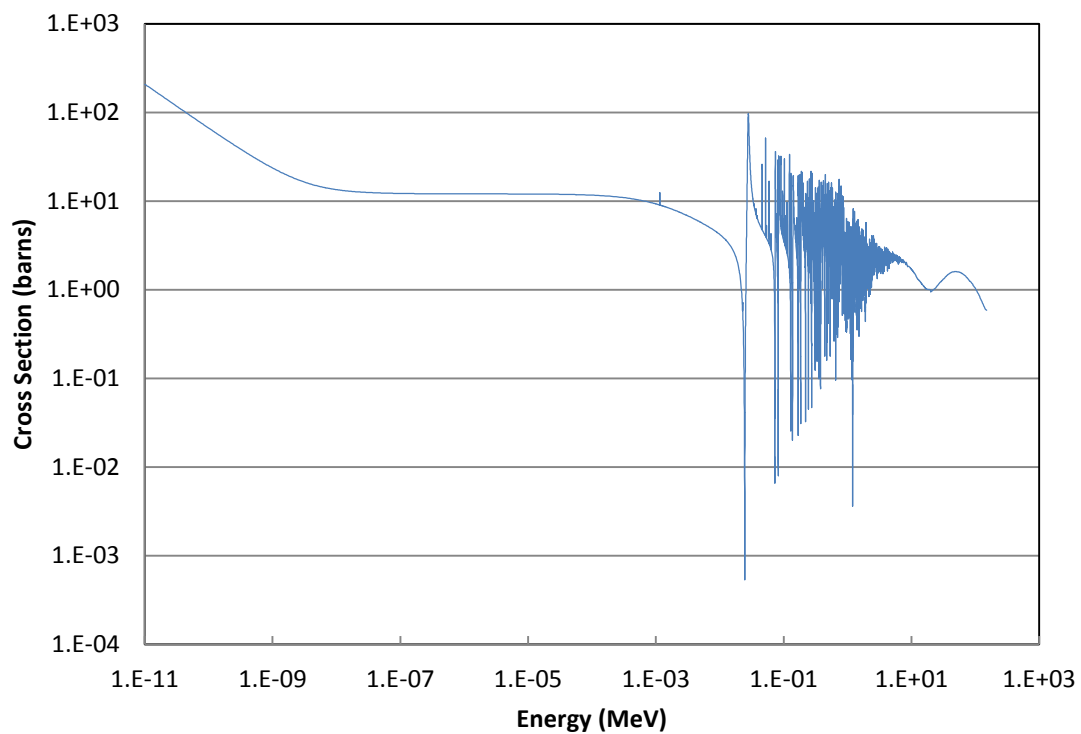


Figure I-8 Total Cross Section of  $^{56}\text{Fe}$  at 1500K

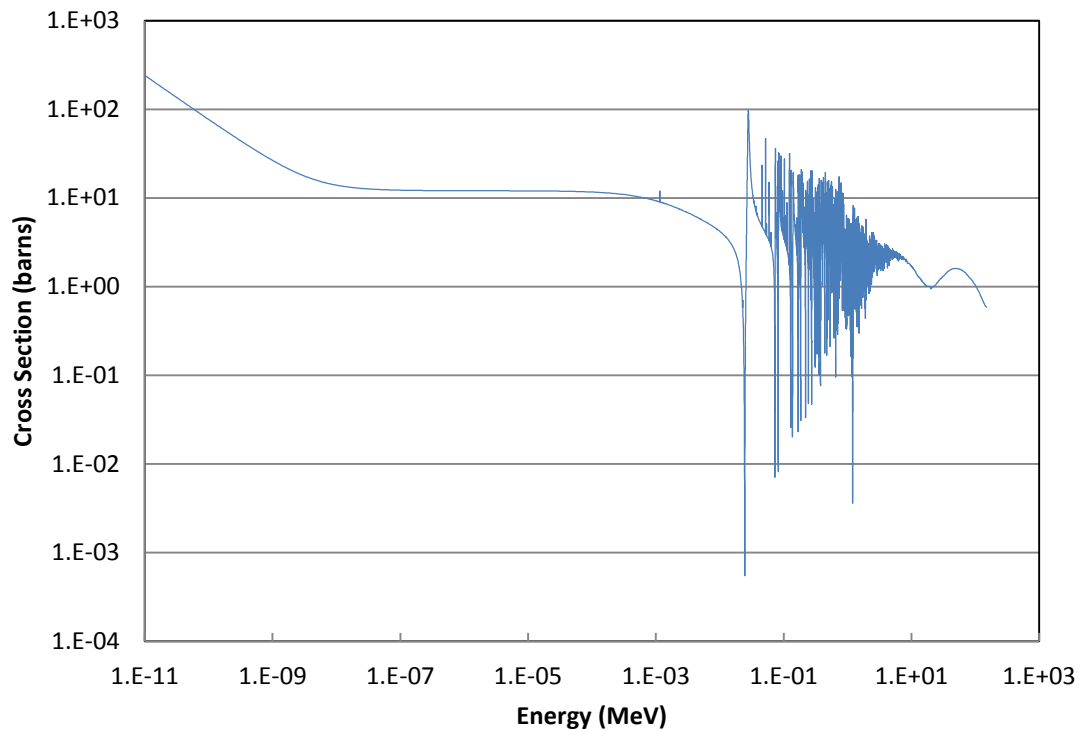


Figure I-9 Total Cross Section of  $^{56}\text{Fe}$  at 2011K

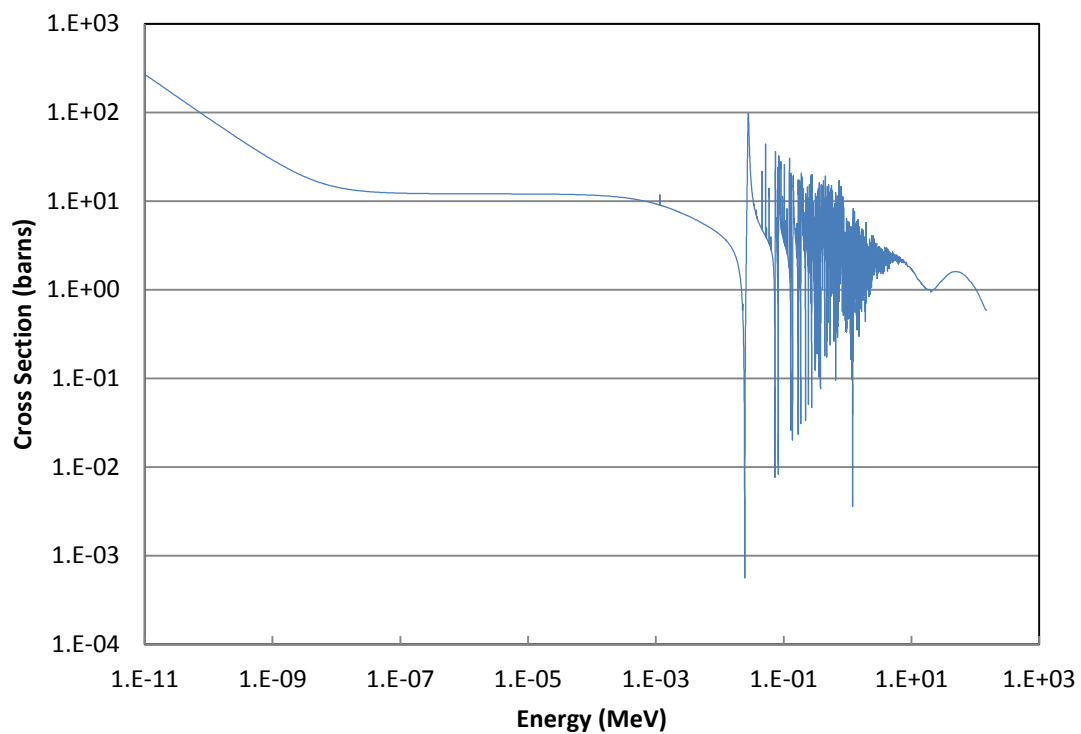


Figure I-10 Total cross section for  $^{56}\text{Fe}$  at 2500K

## 5) References Cited

1. Hodgson, P.E. "The Nuclear Optical Model." *Rep. Prog. Phys.*, 34, 765 (1971).
2. Hauser, Walter, and Herman Feshbach. "The Inelastic Scattering of Neutrons." *Physical Review* 87.2 (1952).
3. Blatt, John Markus., and Victor Frederick Weisskopf. *Theoretical Nuclear Physics*. New York: Dover Publications, 1991. Print.
4. Dietrich, Frank S. *Simple Derivation of the Hauser-Feshbach and Weisskopf-Ewing Formulae, with Application to Surrogate Reactions*. Tech. Lawrence Livermore National Laboratory, 7 Jan. 2004.
5. Herman, M., and A. Trkov. "ENDF-6 Formats Manual." MS. <http://www.jcprg.org/>. Brookhaven National Laboratory, June 2009.
6. Young, P. G., M. B. Chadwick, et al. (2007). "Evaluation of neutron reactions for ENDF/B-VII: U232-241 and Pu-239." *Nuclear Data Sheets* **108**(12): 2589-2654.
7. Shibata, K., T. Kawano, et al. (2002). "Japanese evaluated nuclear data library version 3 revision-3: JENDL-3.3." *Journal of Nuclear Science and Technology* **39**(11): 1125-1136.
8. H. R. Trellue, R. C. Little, and M. B. Lee, "The Processing of ENDF70 and ENDF70PROT: New ACE-Formatted Neutron and Proton Libraries Based on ENDF/B-VII.0, Los Alamos National Laboratory report LA-UR-08-1999.

## **II. Small Scale MCNP runs**

### **1) Introduction**

Three MCNP5 simulations were run using different material inputs. In each simulation, a ball of radius 15.67 centimeters with 80%  $^{235}\text{U}$  and 20%  $^{56}\text{Fe}$  was analyzed to see how the criticality changed over temperature. The material inputs were modified over a temperature range and modified by manually changing some of the data files. The purpose of this test was twofold. First, the temperature dependence of the cross sections was analyzed to show how temperature variations yield different results of criticality. Second, the test was done to show how modifying the cross sections manually would change results of criticality. There were three different tests conducted, which are described below.

### **2) Description of methods**

For the first method, I essentially copied and pasted the previous input deck, but made sure that it read the new cross section file. This cross section file was interpolated using MAKXSF from 293.6 K (which is what the original ENDF tape is at) to 313.6 K, 500 K, 800 K, 1500 K, and 2011 K. These were compared along with the temperature-dependent cross section files included in MCNP were run as well at 293.6K, 600 K, 900K, 1200K and 2500K.

With the second method, the original  $^{56}\text{Fe}$  ENDF elastic scattering cross section was manually changed to a value of 5 barns for all of the energies. From here, the file was modified to the 10 temperatures from method 1 using NJOY99. These files were then used in MCNP to determine how the criticality changed not only by temperature, but how the criticality was changed from Method 1.

For the third method, the ENDF file for  $^{56}\text{Fe}$  was thermally expanded to the 10 temperatures from Method 1. Then the elastic scattering cross sections were manually changed to a value of 5 barns for all energies. These files were then used in MCNP to determine how the criticality changed not only by temperature, but how the criticality was changed from Method 1.

### **3) Results**

Plots of these results are shown on the subsequent pages. Fig. (1) shows the results for Method 1, Fig. (2) shows the results for Method 2 and Fig. (3) shows the results for Method 3.

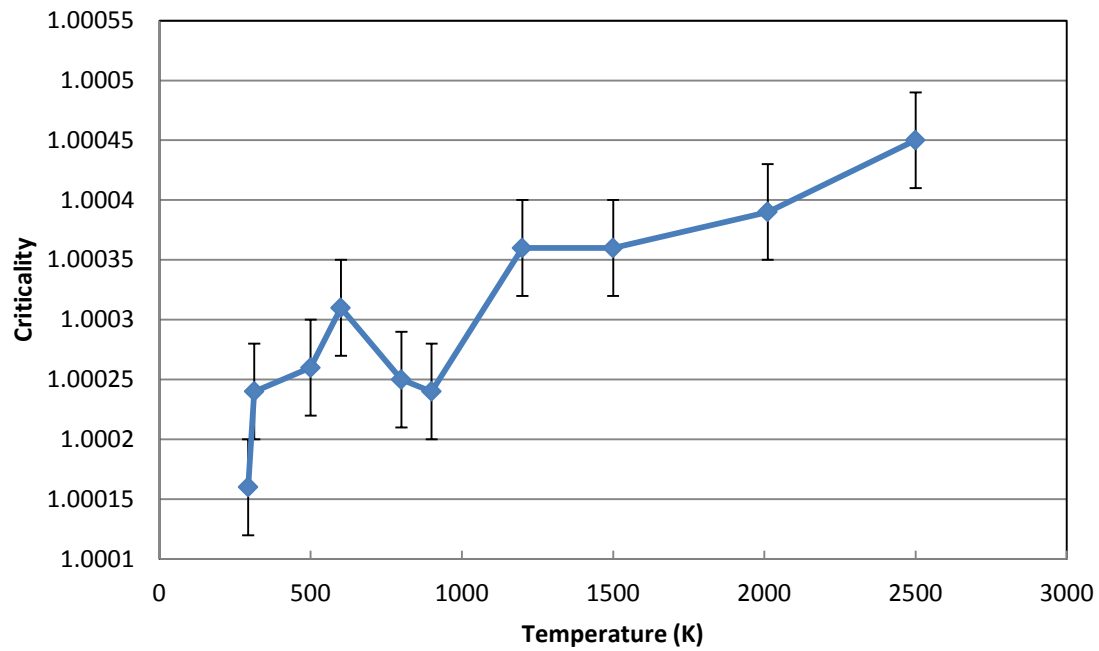


Figure II-1 Method 1 shows little dependence on temperature until higher temperatures are reached

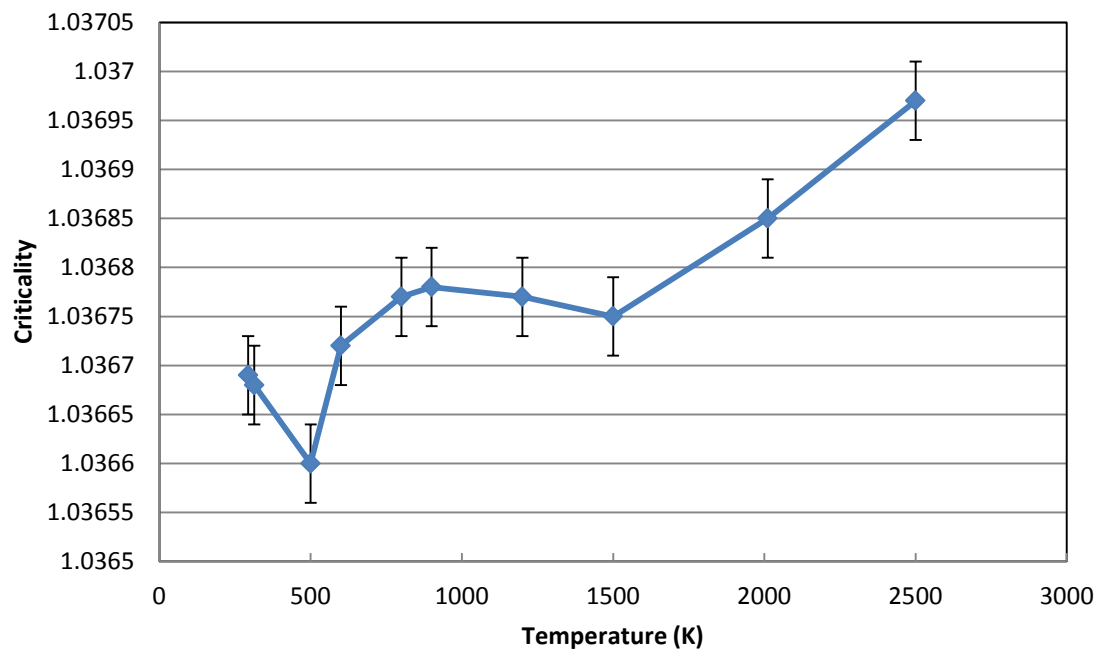


Figure II-2 Method 2 also shows little dependence on temperature until higher temperatures are reached.

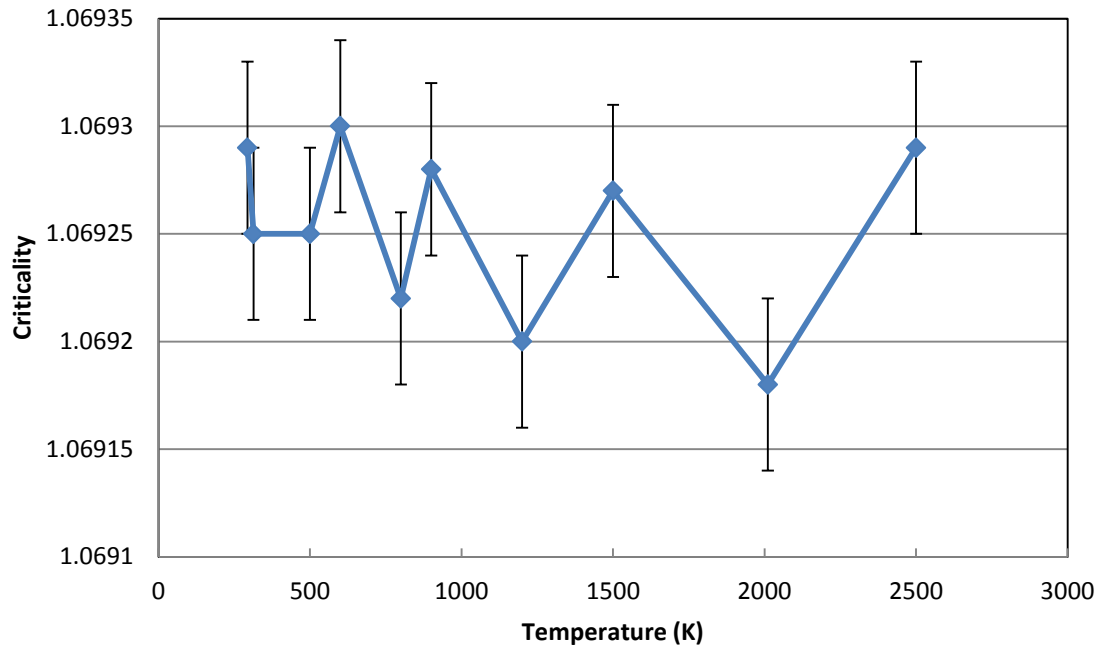


Figure II-3 Method 3 shows almost no dependence on temperature.

#### 4) Analysis

Looking at solely at Method 1, it can be shown that the total range of  $K_{eff}$  spans a range of  $3E-4$ , which is not insignificant since the only variable changed was the temperature.

Analyzing all of the Methods shows how modifying the data file can have a huge impact on the  $K_{eff}$  of the sphere. The forms of Methods 1 and 2 agree with each other more so than with Method 3 and the only relation between Methods 1 and 2 occurs at higher temperatures (above 1200K). The  $k_{eff}$  in both methods increases with temperature for the high temperature regime. There is no apparent correlation in Method 3 with temperature or the other two methods. This is to be expected, as the elastic cross section was modified after it was thermally expanded and reads at directly 5 barns, which has almost no physical significance.

# III. Full Scale Reactor Models in MCNP

## 1) Introduction

A baseline was run for the Westinghouse AP1000 and VHTR using MCNPX. The purpose of this was to calculate the keff, neutron flux, total reaction rate (RR), elastic scattering RR, inelastic scattering RR and energy deposition over several burnup times at several locations throughout each core. The data from the MCNPX runs and the plots generated in this report will be used as a baseline for comparison once modifications to the nuclear data files are made.

Once these modifications are made to the data files, the following will

The reaction rates are calculated in MCNP by the FMn card using

$$RR(E) = C \int \varphi(E)\sigma(E)dE \quad (3.1.1)$$

where  $RR(E)$  is the energy-dependent reaction rate in [n/s],  $C$  is an arbitrary constant that can be used for normalization,  $\varphi(E)$  is the energy-dependent flux in [n/cm<sup>2</sup>/s] and  $\sigma(E)$  is the energy-dependent microscopic cross section in [cm<sup>2</sup>]. In this case,  $C$  would be unitless. Even though the FMn card can be used to calculate reaction rates of unique combinations of reactions, the cards used in this code were only of an individual reaction.

## 2) AP1000 and VHTR Descriptions

The AP1000 is a Gen III+ 3400 MW thermal PWR. The input deck was run with fuel rods of 2.95% weight-enriched <sup>235</sup>U with a Zircaloy cladding. The tallies were taken from the meat of the 2.95% enriched fuel rod and the associated fuel assembly. Burnup time steps start at 10 days, then are taken at time intervals of 100 days until the end of life of the core. The time steps are then increased to 1825 days to simulate how the fuel rods will behave while they are in storage outside of the core.

The and tallied over the fuel region of a fuel rod and fuel assembly.

The VHTR input deck tallied over four different positions: a TRISO fuel particle with 8% enrichment, the fuel region of a fuel compact rod, a fuel block and throughout the entire core.

## 3) Modifications to Data Files

Once the initial test run finishes, the MCNP data files are manipulated using a custom-written FORTRAN code. The code reads the ACE format data file and changes the value of the elastic scattering cross

section to whatever the user desires. For this test, the cross sections for the largest-contributing nuclide in the fuel rods were changed to a constant value. For the AP1000, the elastic scattering cross section for  $^{238}\text{U}$  was changed to 9.5 barns over all energy ranges. For the VHTR, the elastic scattering cross section for  $^{239}\text{Pu}$  was changed to 9.0 barns.

#### **4) Results**

The data for the runs are shown on the subsequent pages in Figs. 1-6. A more detailed version of each plot is shown in Appendix A.



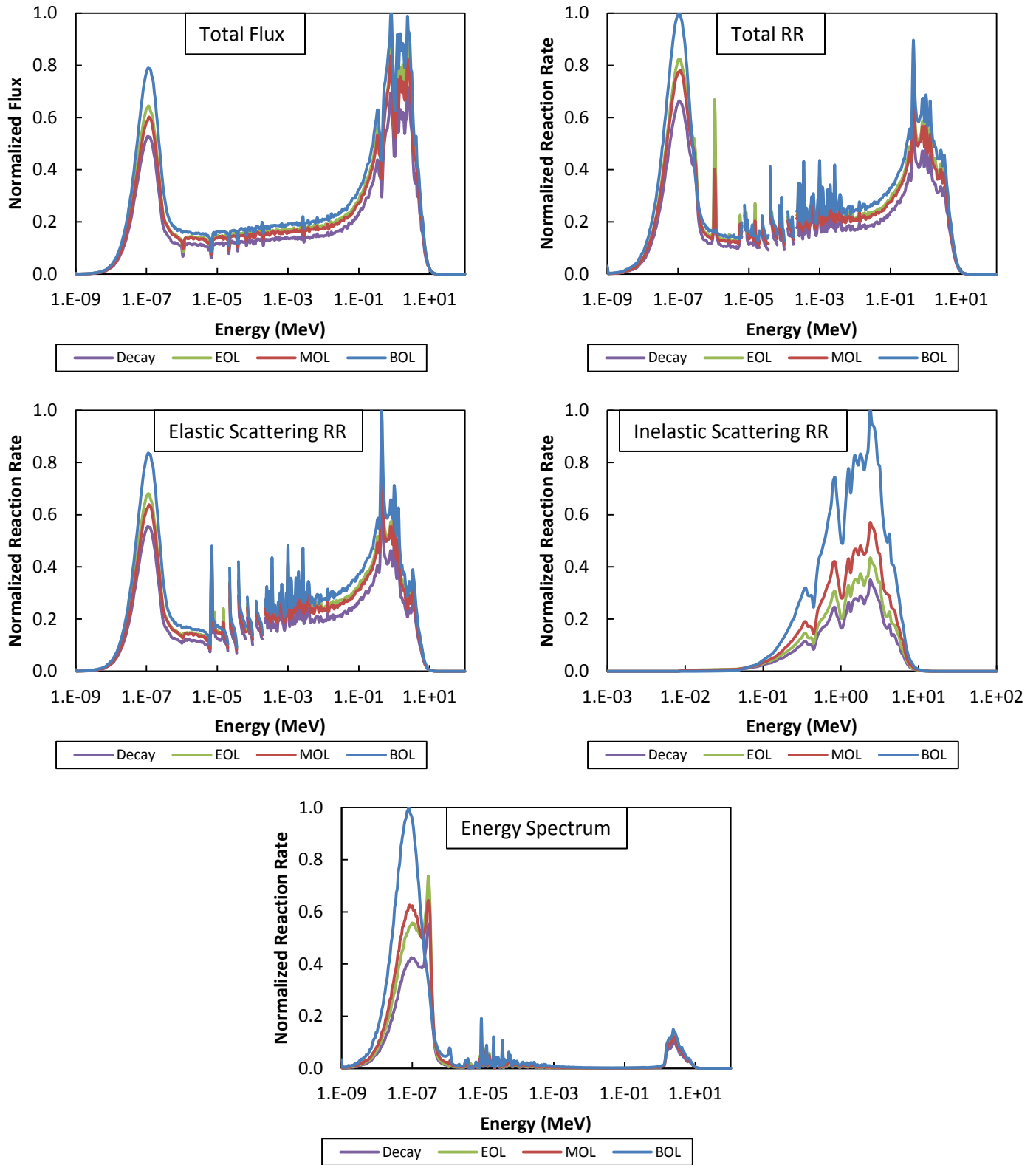


Figure III-1 For the AP1000 fuel assembly, all of the values decrease as time goes on with the exception of some of the randomness in the total RR, elastic scattering RR and energy spectrum. The shapes of these curves are very similar to the ones for a fuel rod in the AP1000. This most likely means that the structural material and water that composes the fuel assembly does not make a major contribution to these calculations.

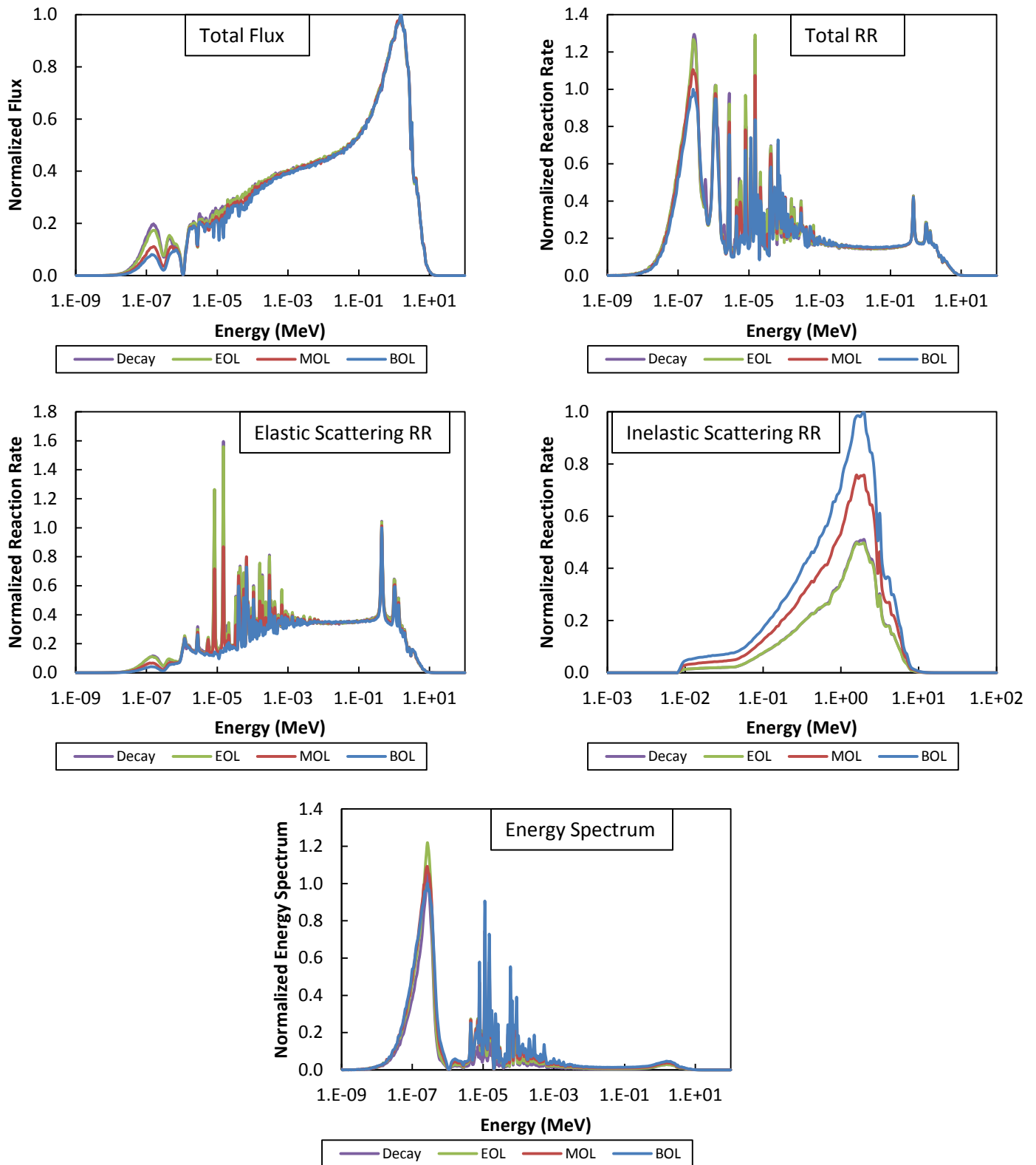


Figure III-2 With a TRISO fuel particle in the VHTR, the total flux, with the exception of the low energy spectrum then shows very little change in time, while the elastic scattering RR shows almost no change with time. Both the total RR and inelastic RR both decrease in time more rapidly during core lifetime, then slightly during the decay time. The energy spectrum increases during core lifetime, then decreases during decay time.

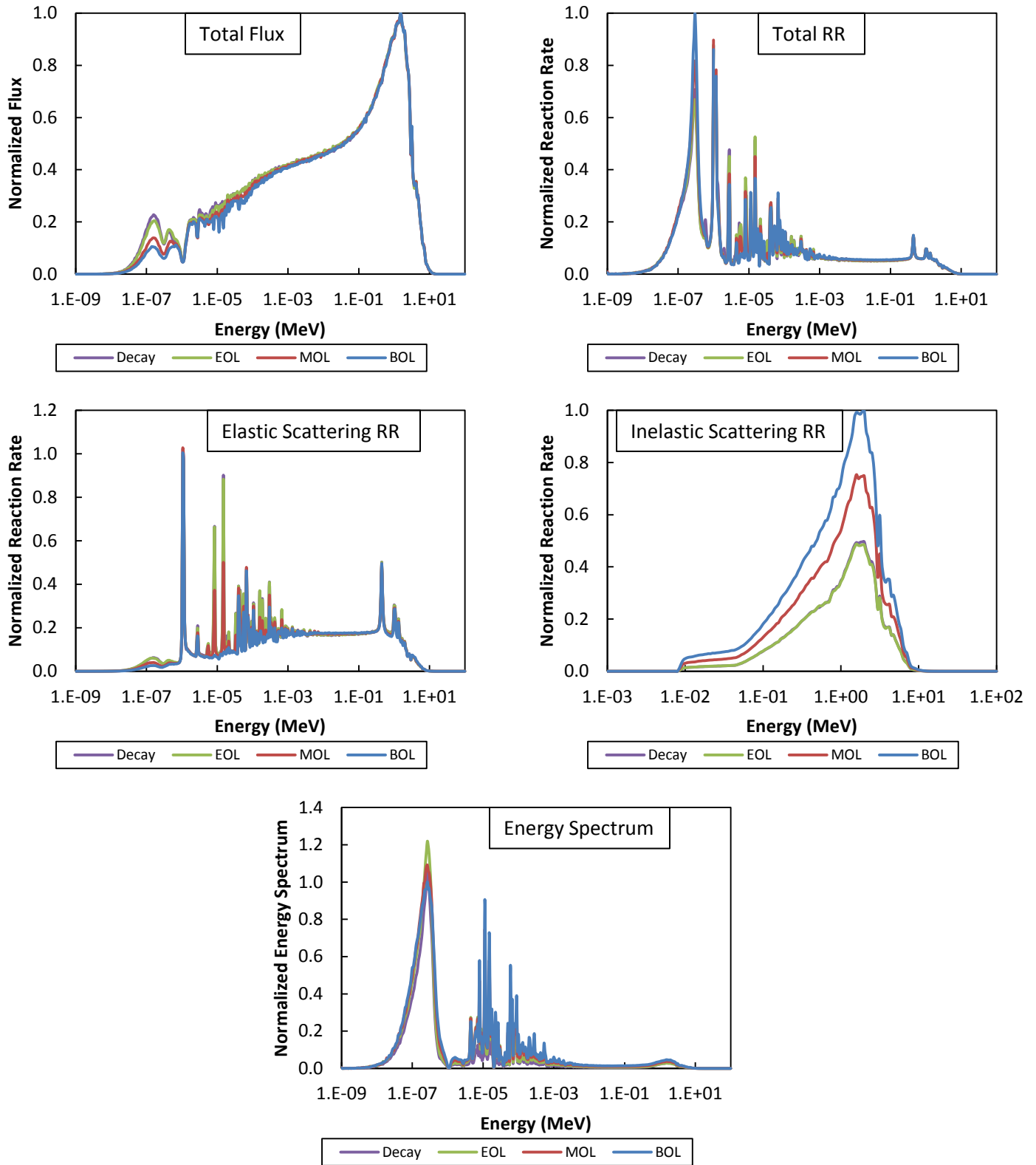


Figure III-3 A fuel rod in the VHTR shows that the total flux shows a slight increase in time at low energies and then is mostly constant with time while the elastic scattering RR shows almost no change with time with the exception of some randomness in the resonance region. Both the total RR and inelastic RR both decrease in time more rapidly during core lifetime, then slightly during the decay time, while the energy spectrum increases during core lifetime, then decreases during decay time.

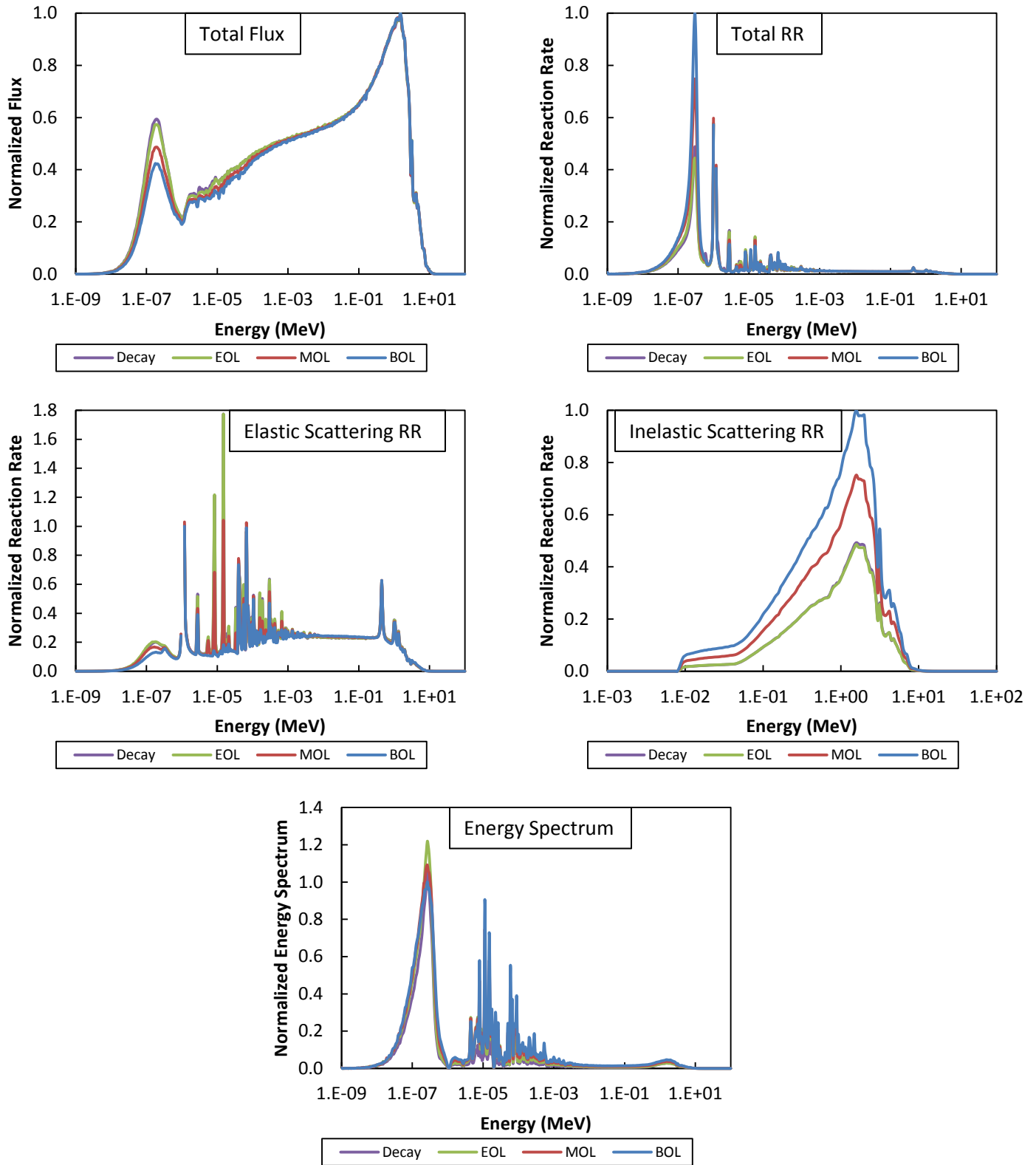


Figure III-4 A fuel block in the VHTR follows a similar result to the fuel rod in the VHTR. Again, the total flux shows a slight increase in time at low energies and then is mostly constant with time while the elastic scattering RR shows almost no change with time. The total RR and inelastic RR both decrease in time more rapidly during core lifetime, then slightly during the decay time. The energy spectrum increases during core lifetime, then decreases during decay time.

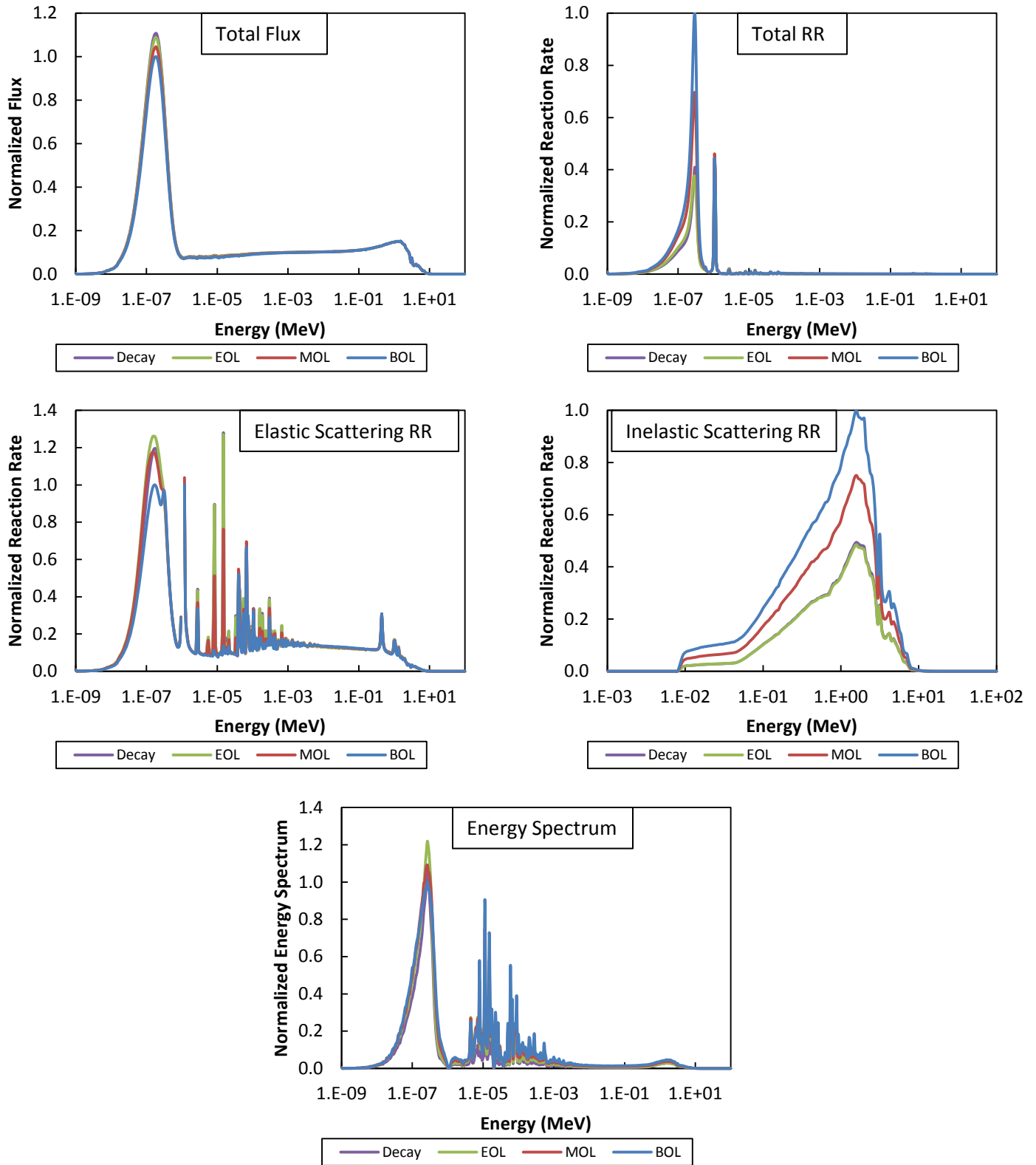


Figure III-5 The whole core in the VHTR differs from the fuel rod on in that the total flux barely changes over time except for the low energy regime, while the elastic scattering RR and energy spectrum values increase throughout the core lifetime then decrease during the decay time. The total RR and inelastic scattering RR continuously decrease with time throughout core lifetime and decay

IV. Appendix A

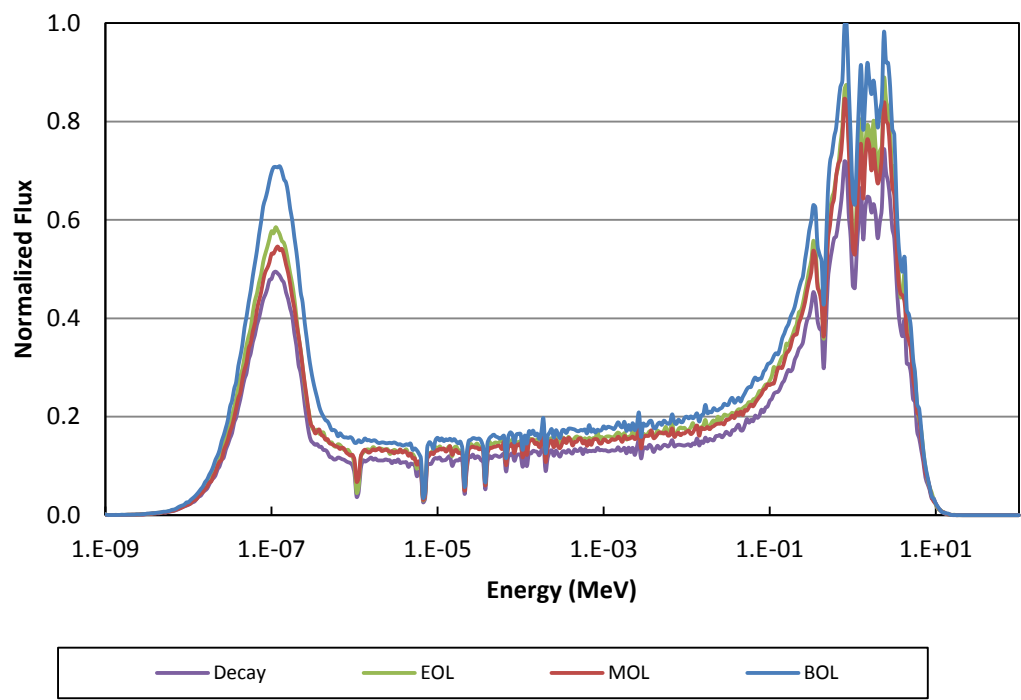


Figure IV-1 Neutron flux of a fuel rod in the AP1000

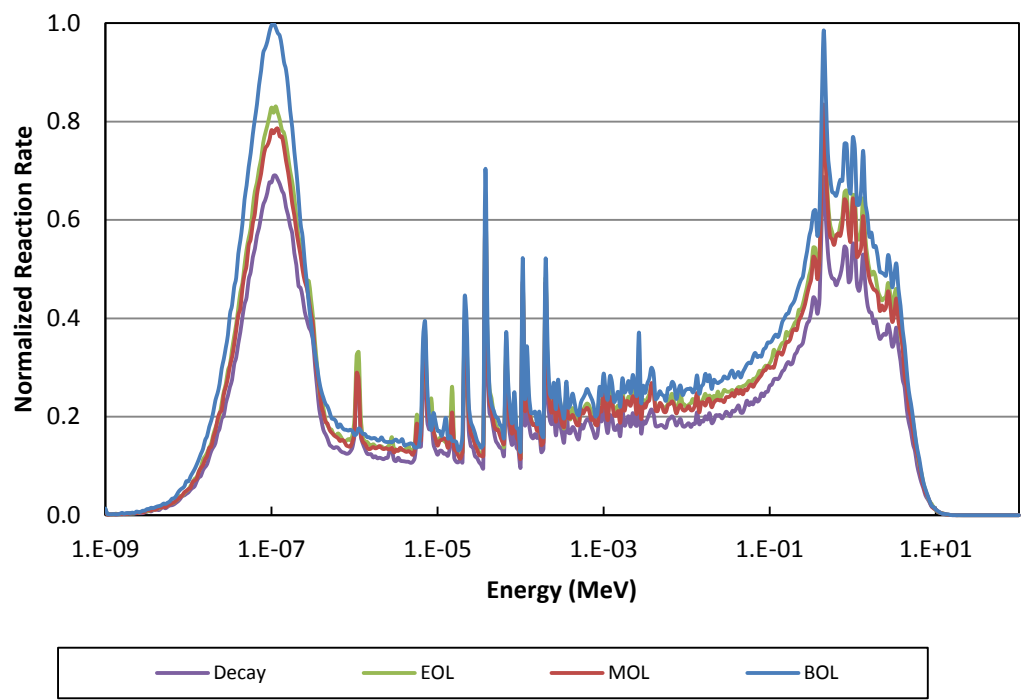


Figure IV-2 Total reaction rate for a fuel rod in the AP1000

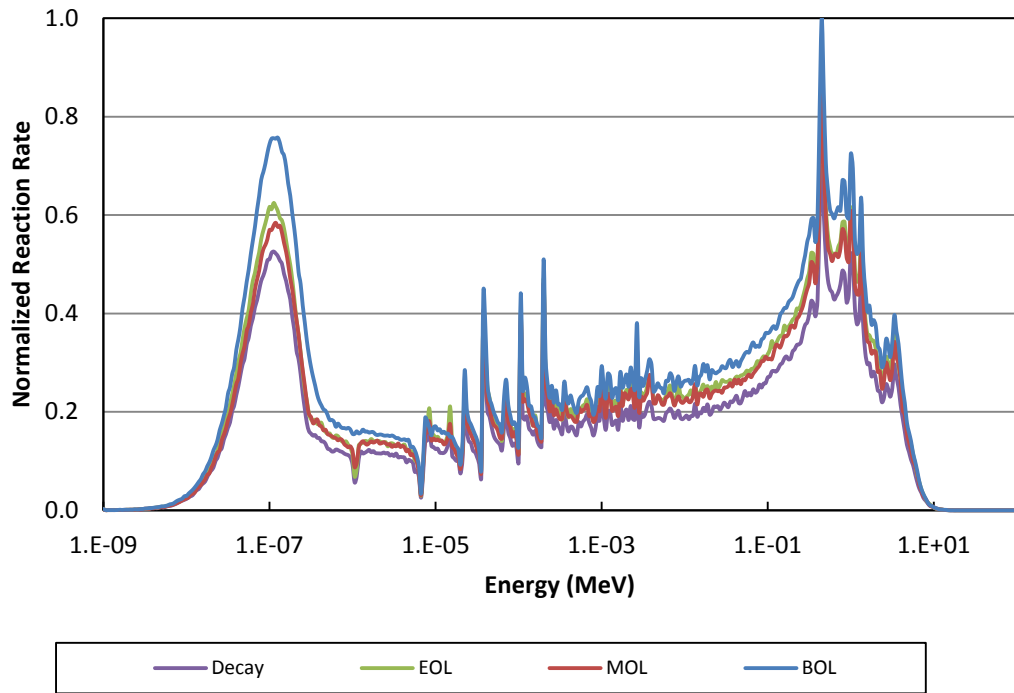


Figure IV-3 Elastic scattering reaction rate for a fuel rod in the AP1000

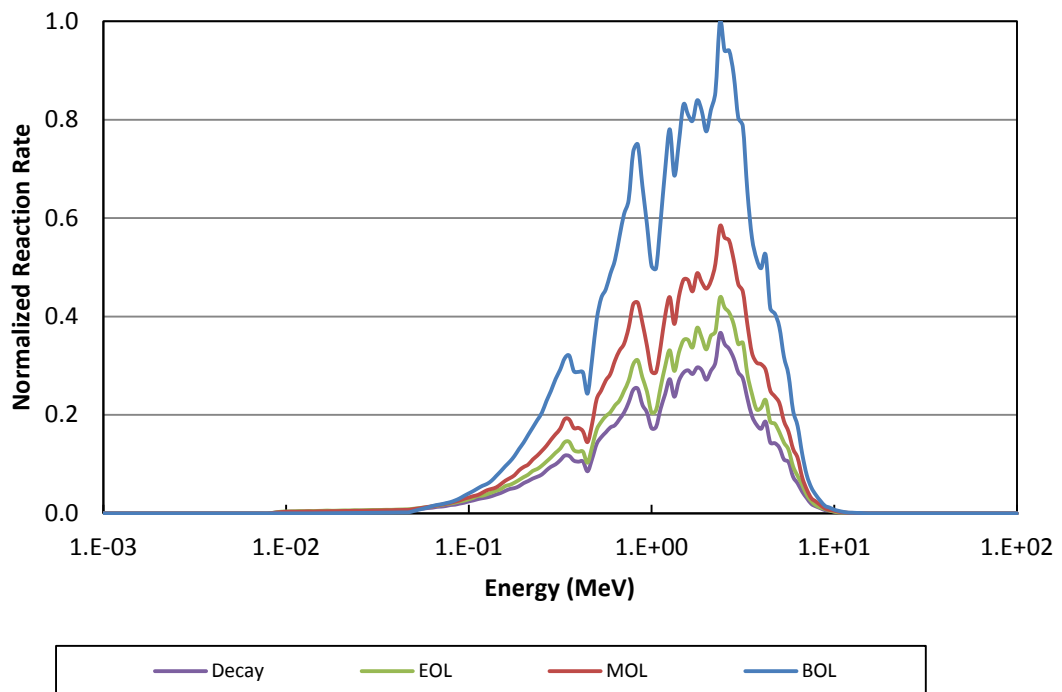


Figure IV-4 Inelastic scattering reaction rate for a fuel rod in the AP1000

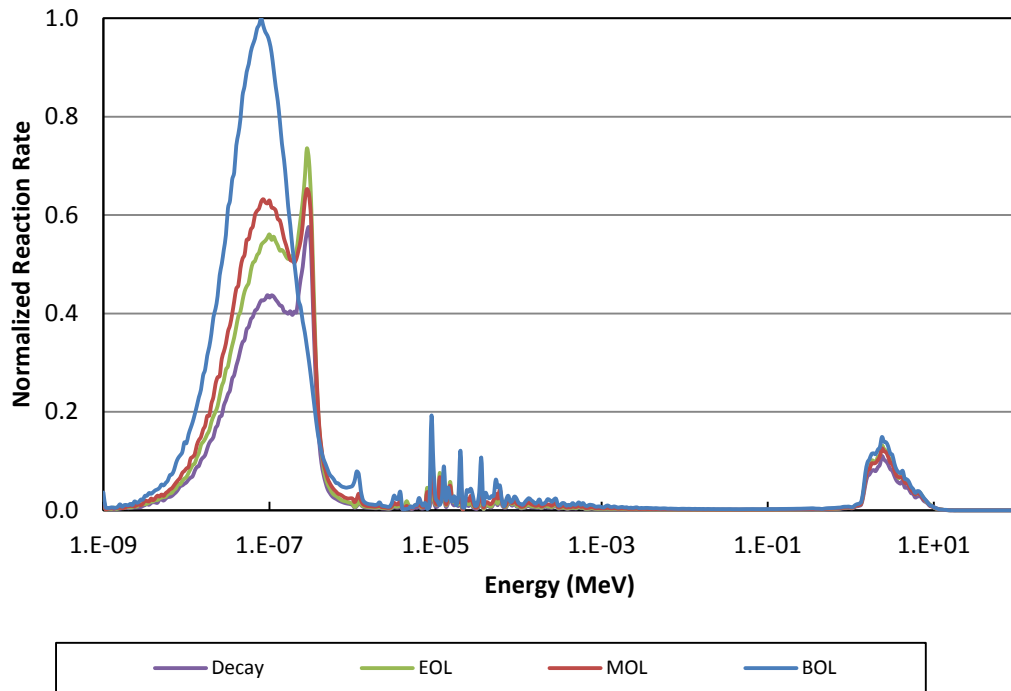


Figure IV-5 Energy deposition averaged over a fuel rod in the AP1000

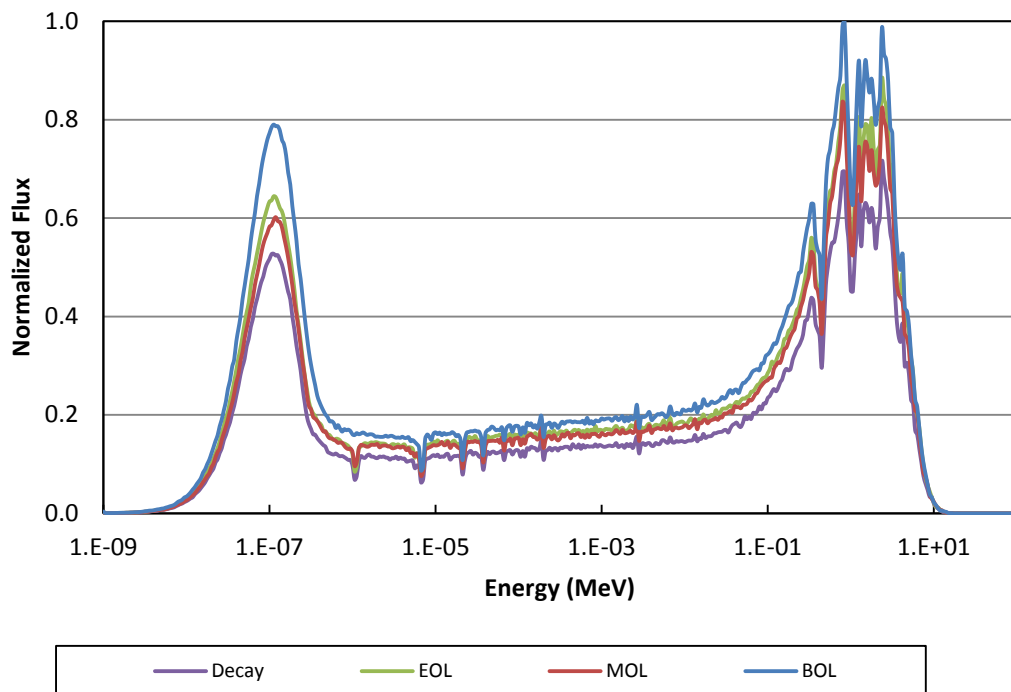


Figure IV-6 Neutron flux of a fuel assembly in the AP1000



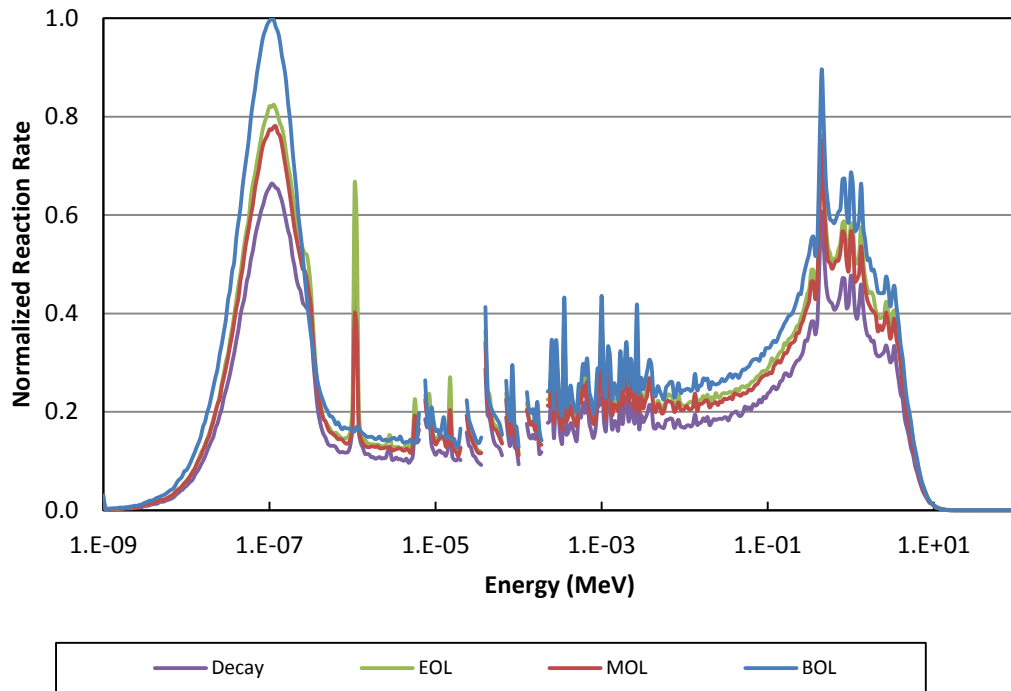


Figure IV-7 Total reaction rate for a fuel assembly in the AP1000

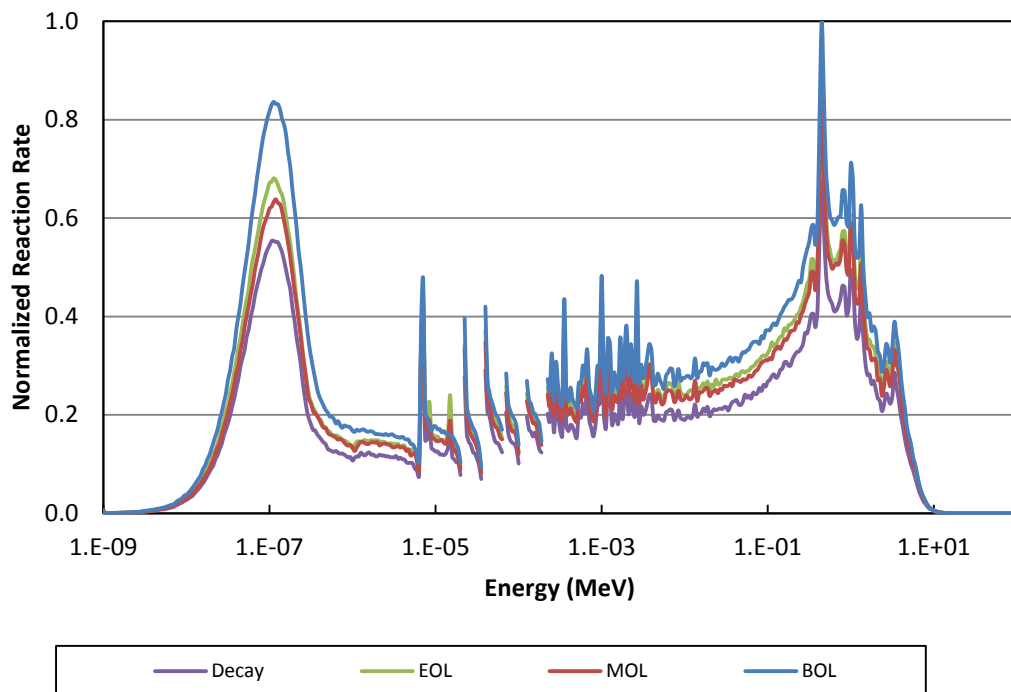


Figure IV-8 Elastic scattering reaction rate for a fuel assembly in the AP1000

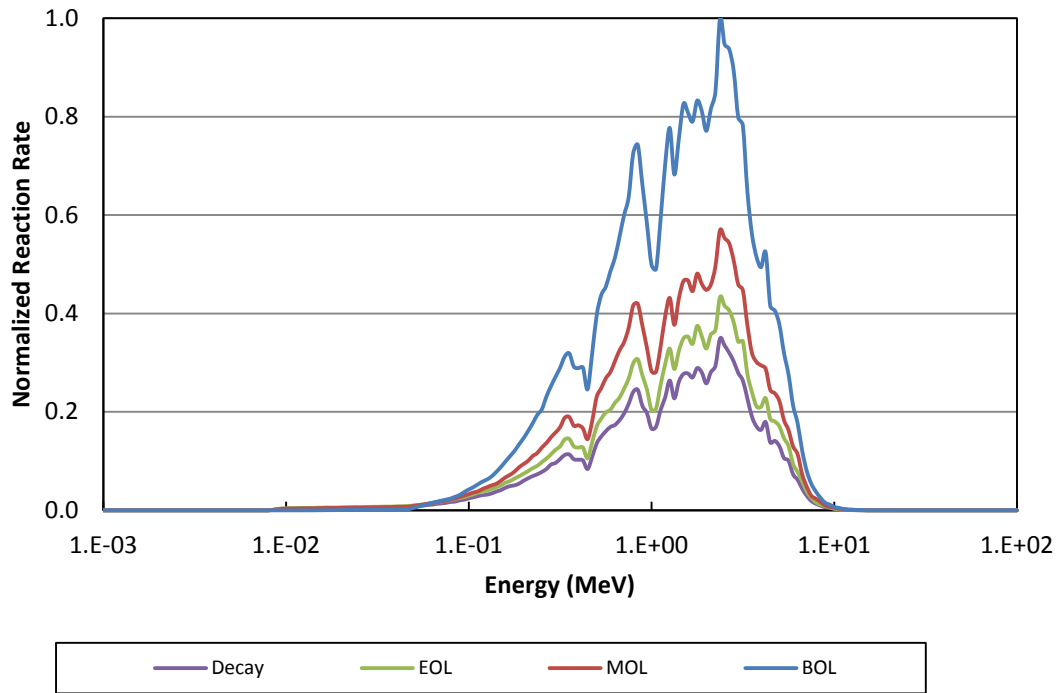


Figure IV-9 Inelastic scattering reaction rate for a fuel assembly in the AP1000

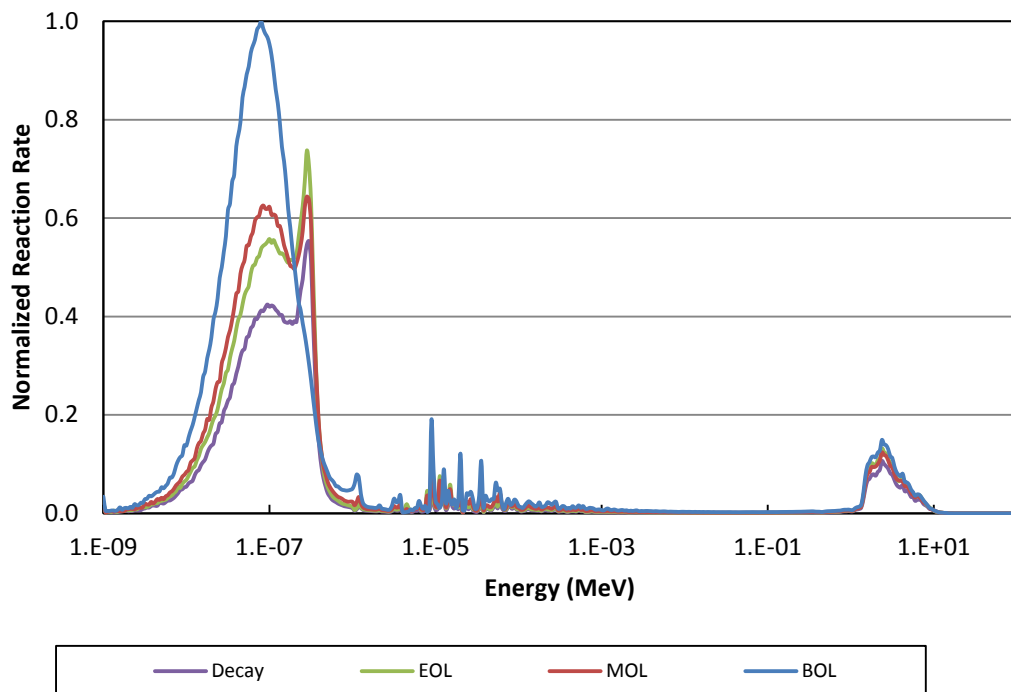


Figure IV-10 Energy deposition averaged over a fuel assembly in the AP1000

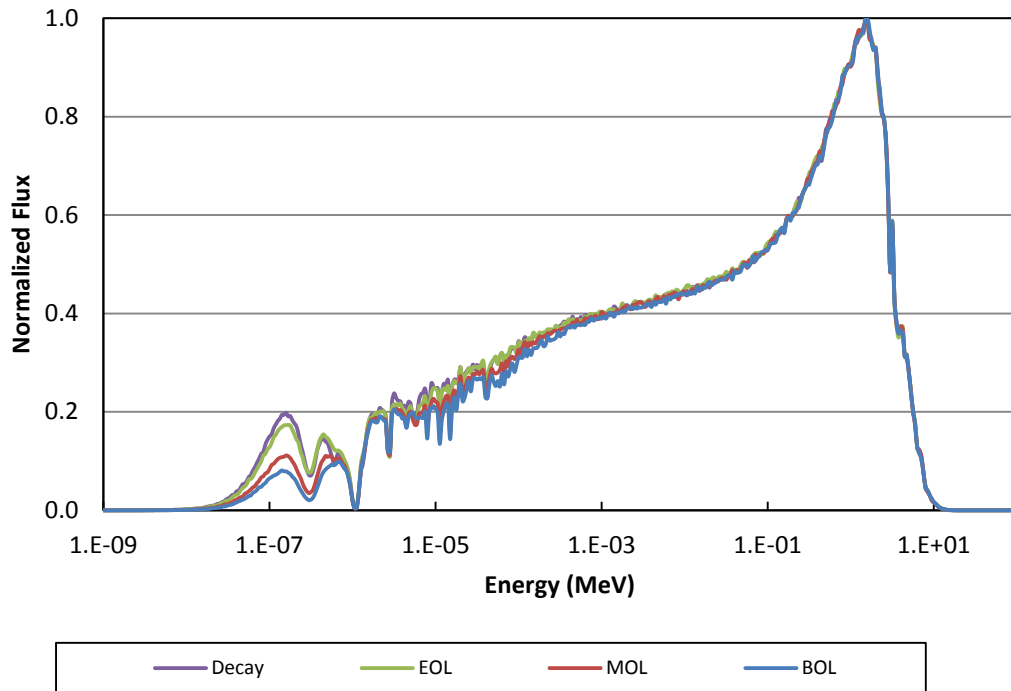


Figure IV-11 Neutron flux of a TRISO fuel particle in the VHTR

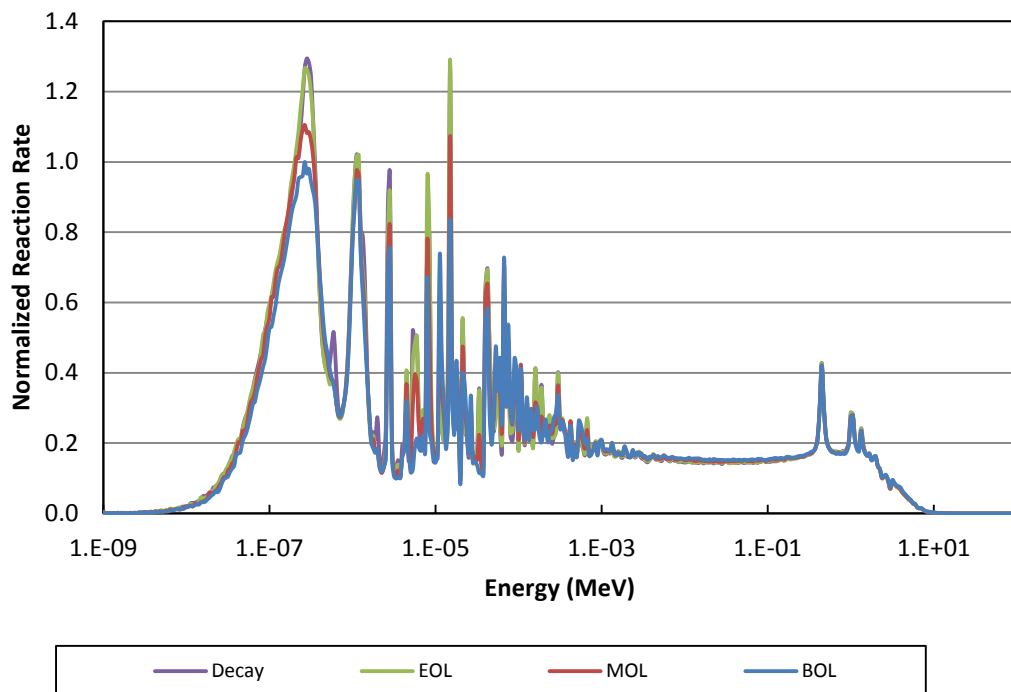


Figure IV-12 Total reaction rate of a TRISO fuel particle in the VHTR

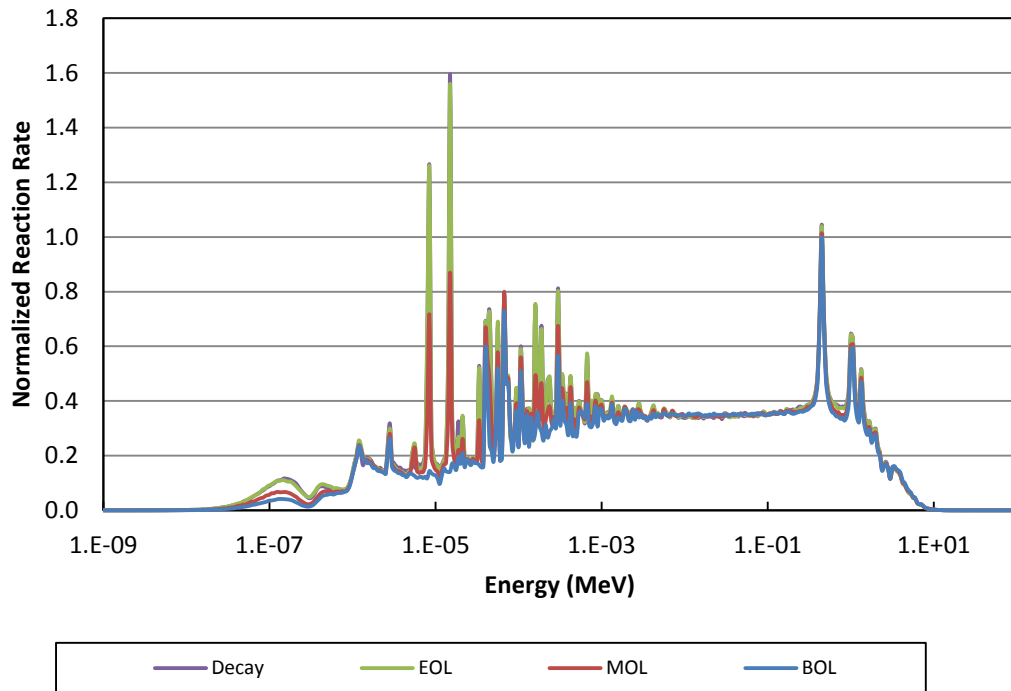


Figure IV-13 Elastic scattering reaction rate of a TRISO fuel particle in the VHTR

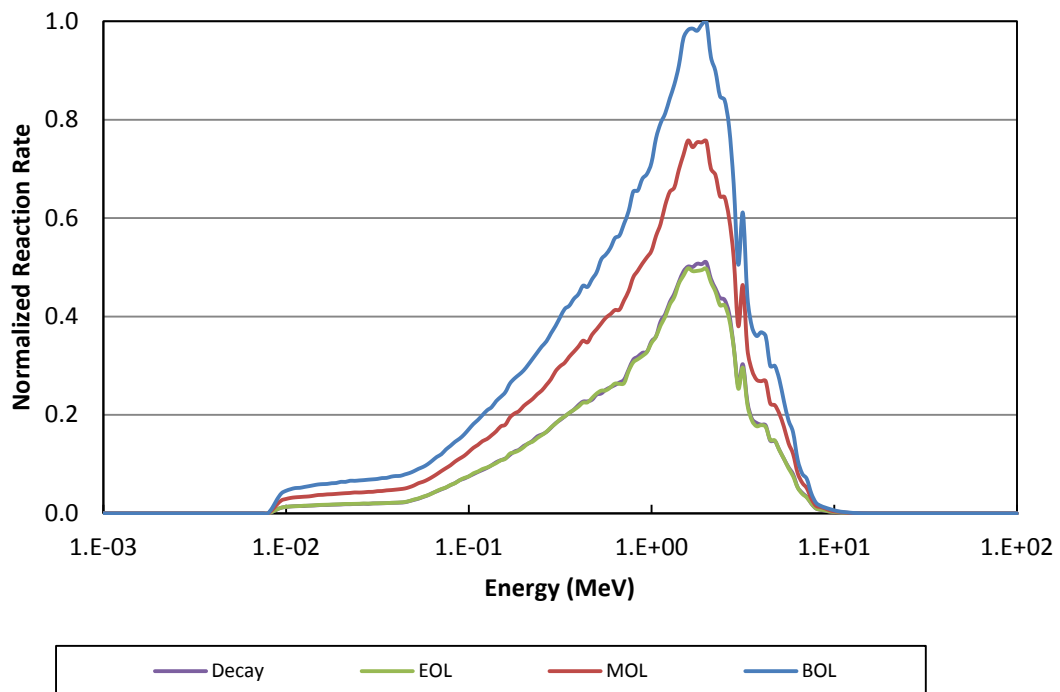


Figure IV-14 Inelastic scattering reaction rate of a TRISO fuel particle in the VHTR

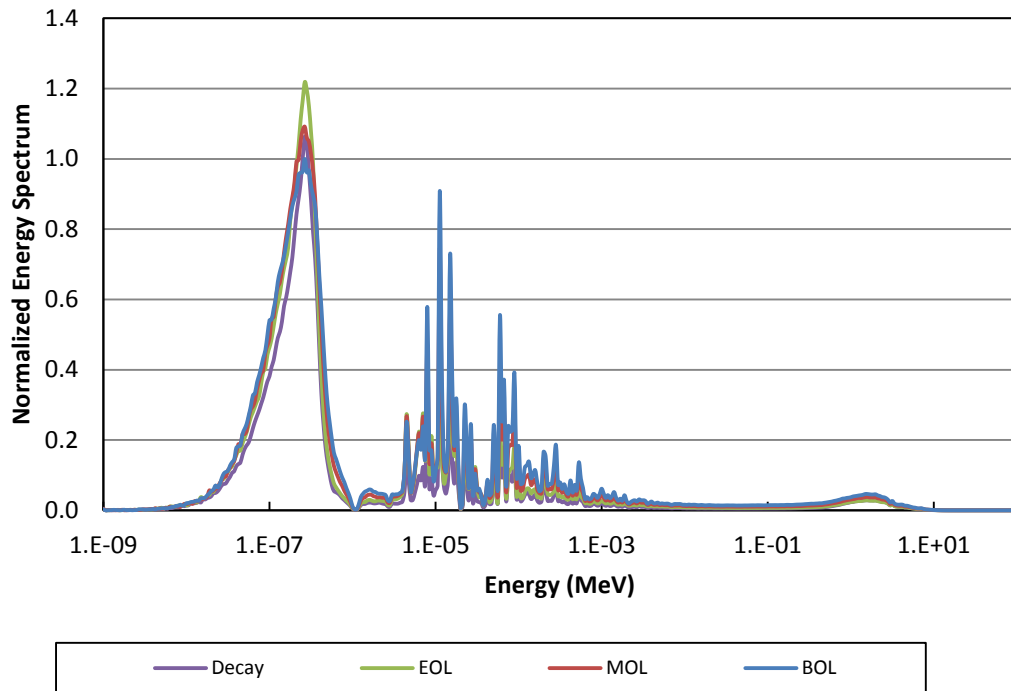


Figure IV-15 Energy deposition averaged over a TRISO fuel particle in the VHTR

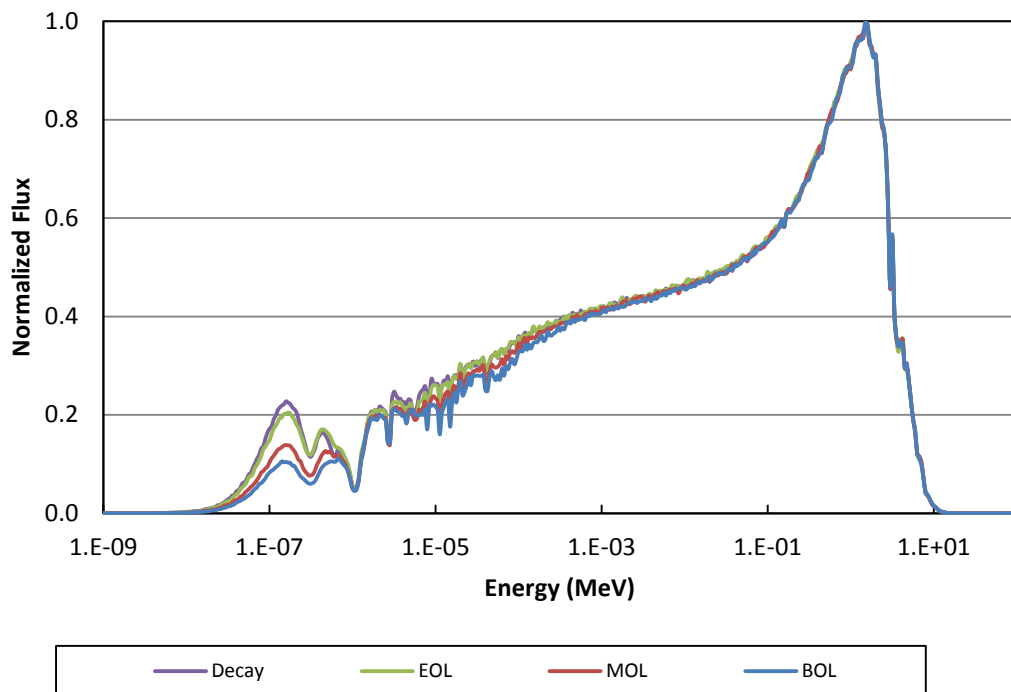


Figure IV-16 Neutron flux of the fuel region of a fuel rod in the VHTR

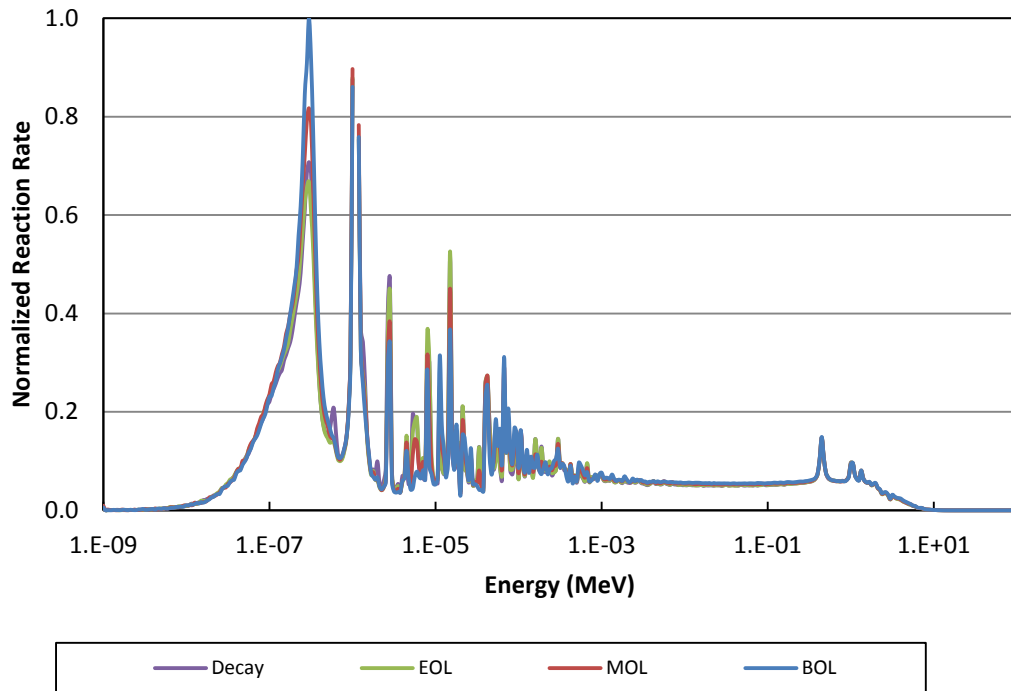


Figure IV-17 Total reaction rate of the fuel region of a fuel rod in the VHTR

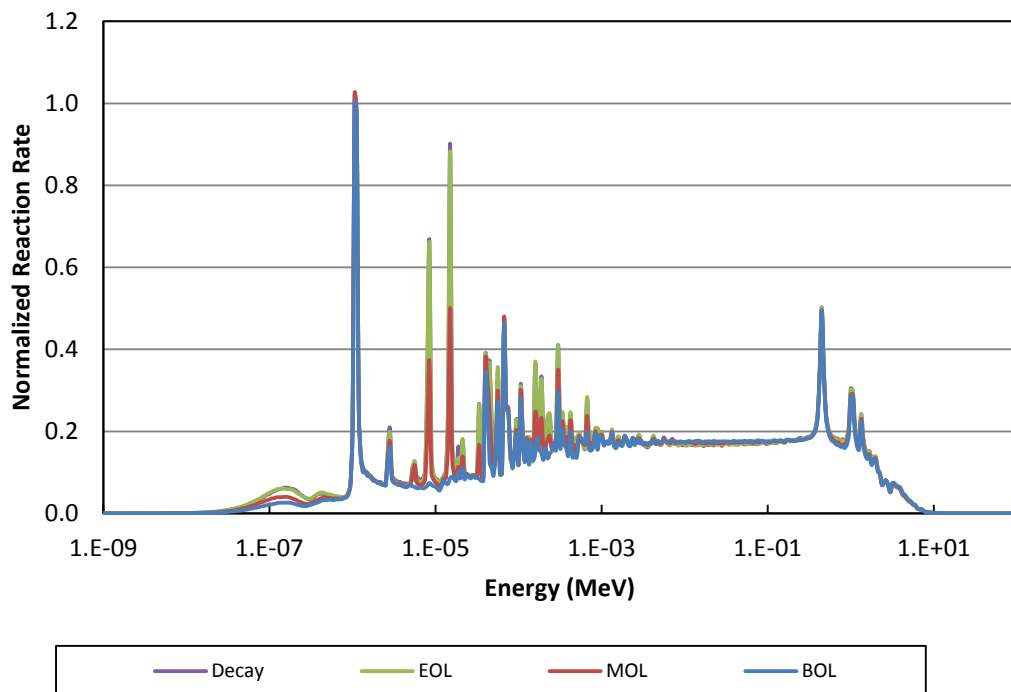


Figure IV-18 Elastic scattering reaction rate of the fuel region of a fuel rod in the VHTR

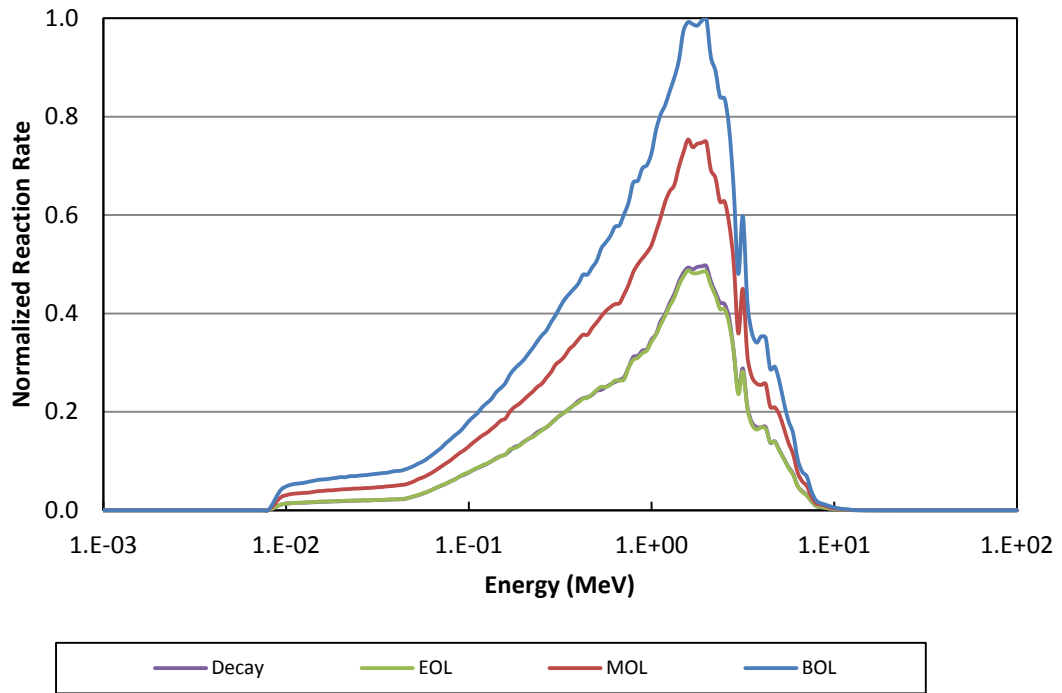


Figure IV-19 Inelastic scattering reaction rate of the fuel region of a fuel rod in the VHTR

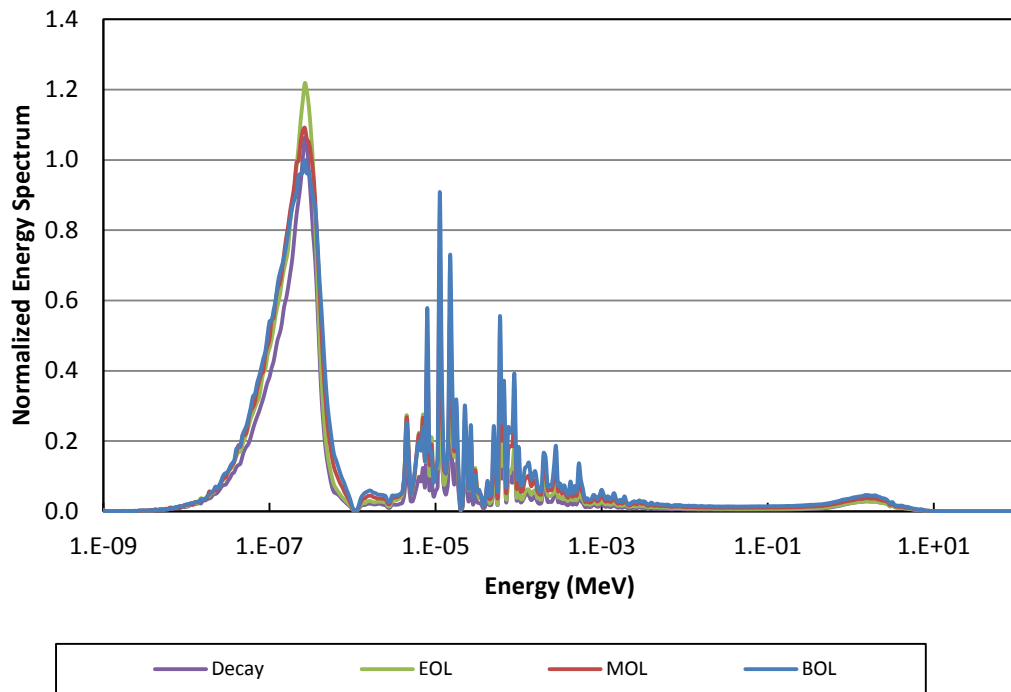


Figure IV-20 Energy deposition averaged over the fuel region of a fuel rod in the VHTR

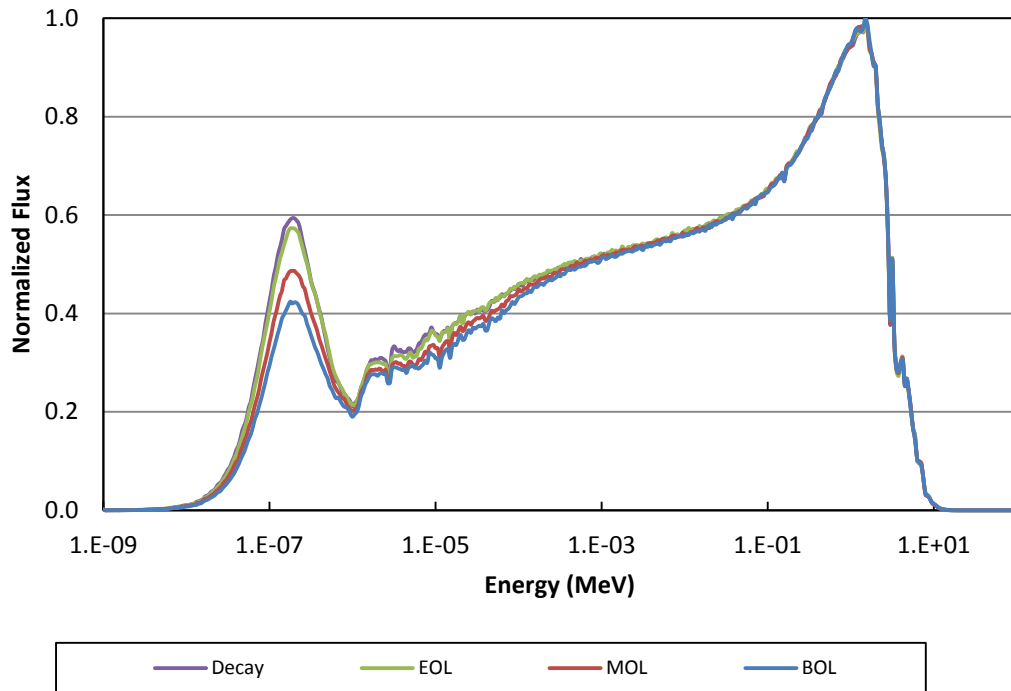


Figure IV-21 Neutron flux of a fuel block in the VHTR

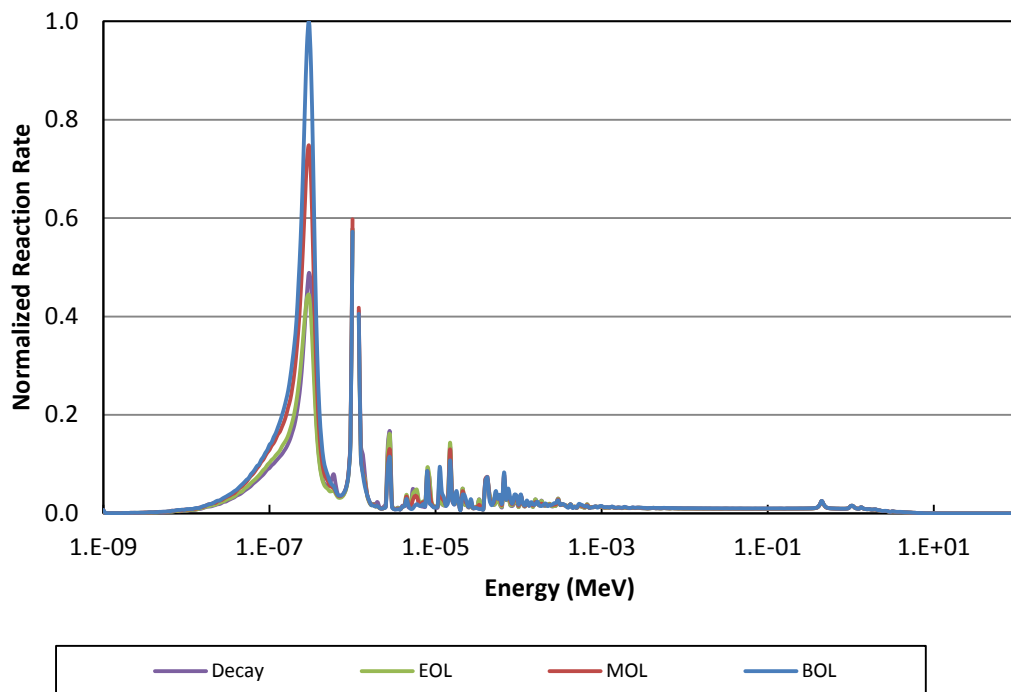


Figure IV-22 Total reaction rate of a fuel block in the VHTR



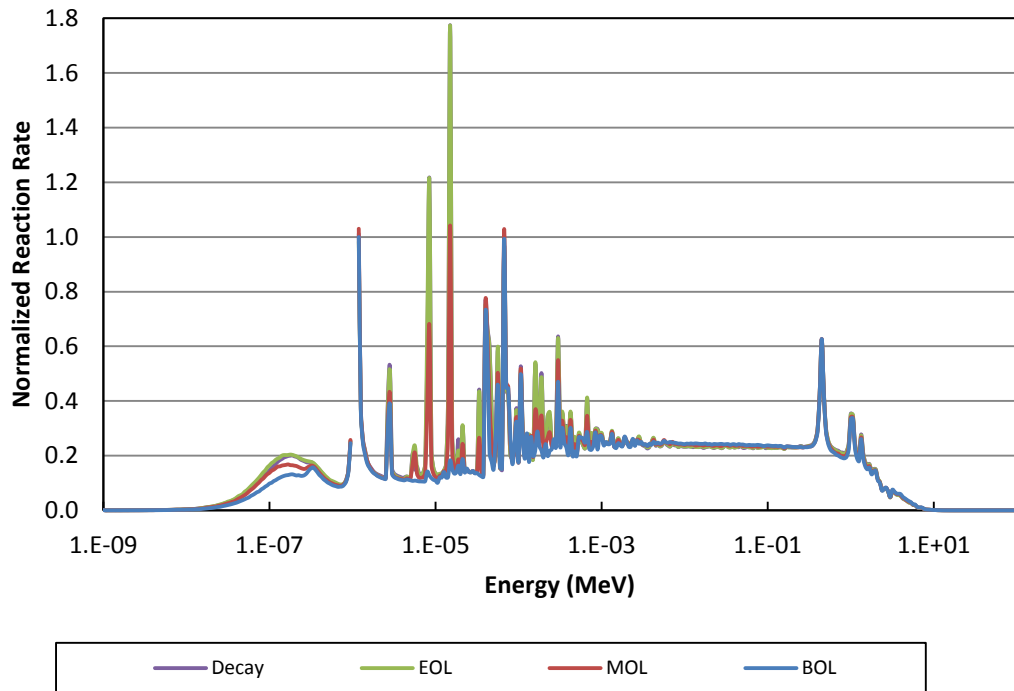


Figure IV-23 Elastic scattering reaction rate of a fuel block in the VHTR

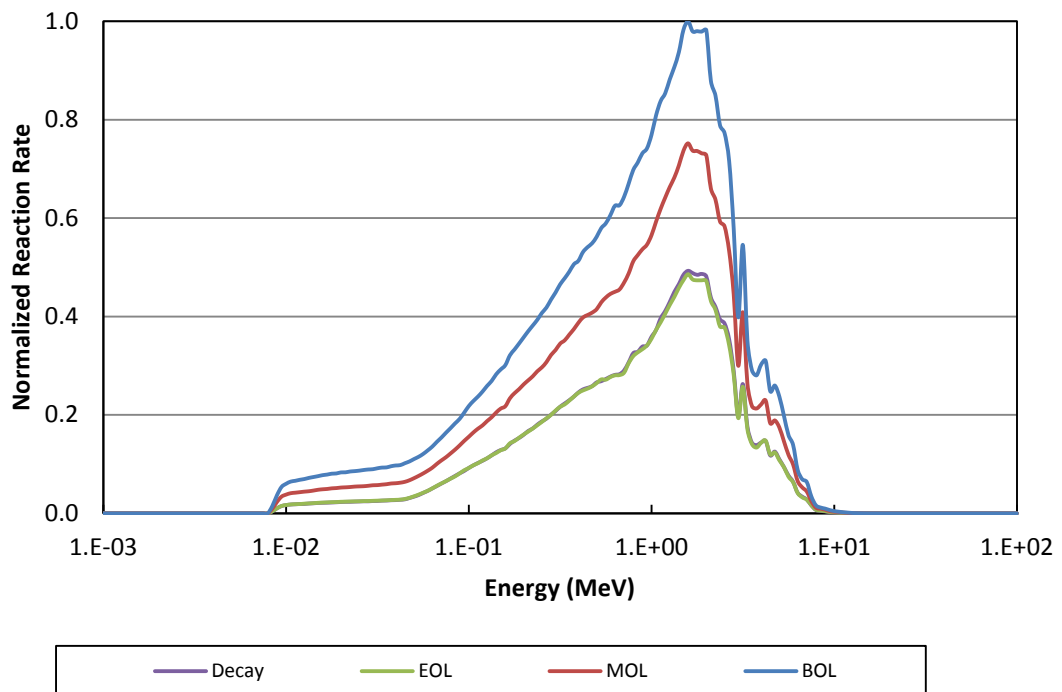


Figure IV-24 Inelastic scattering reaction rate of a fuel block in the VHTR

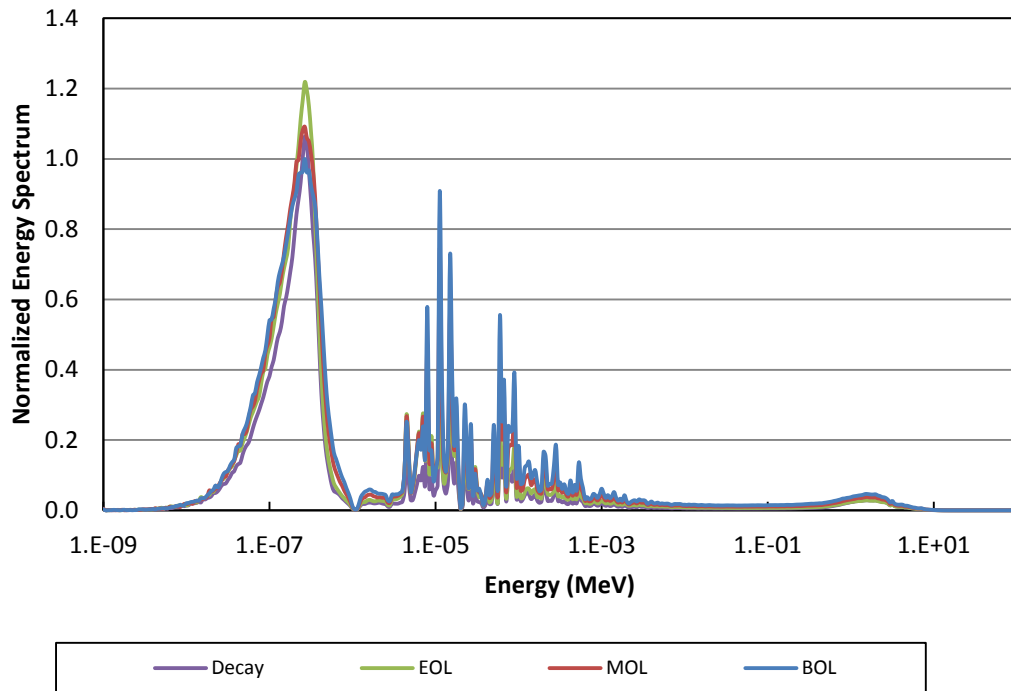


Figure IV-25 Energy deposition averaged over a fuel block in the VHTR

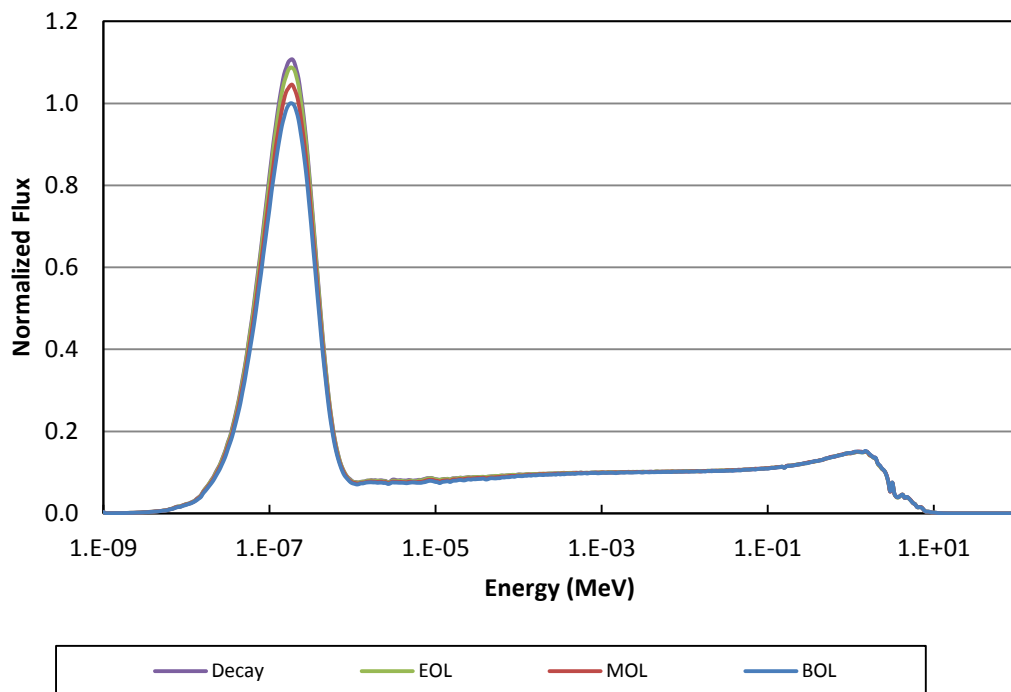


Figure IV-26 Neutron flux of the core of the VHTR

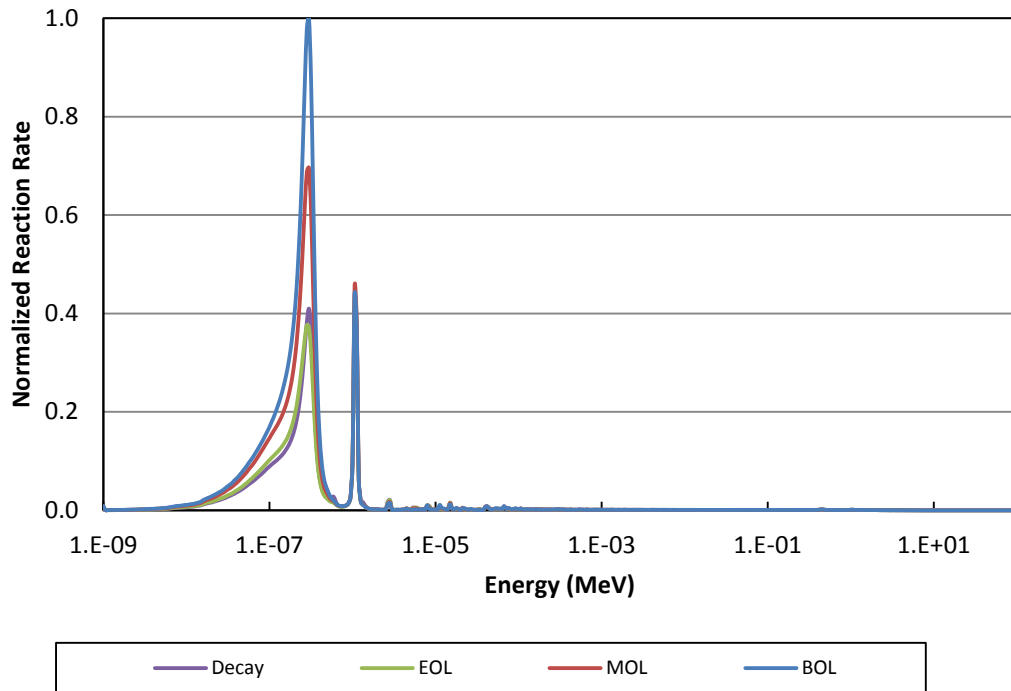


Figure IV-27 Total reaction rate of the core of the VHTR

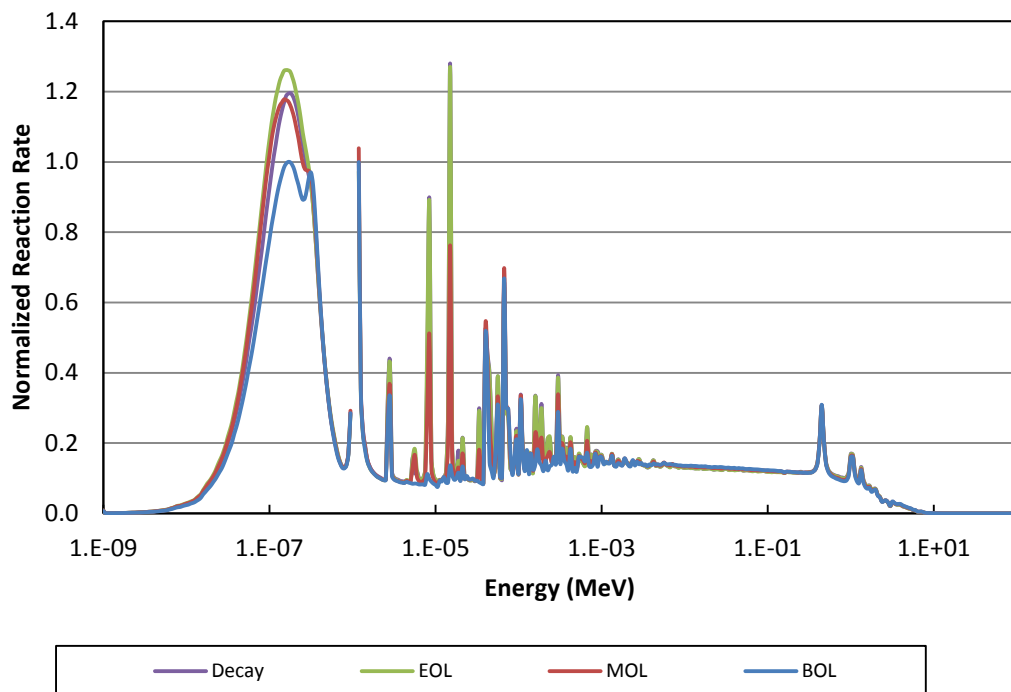


Figure IV-28 Elastic scattering reaction rate of the core of the VHTR

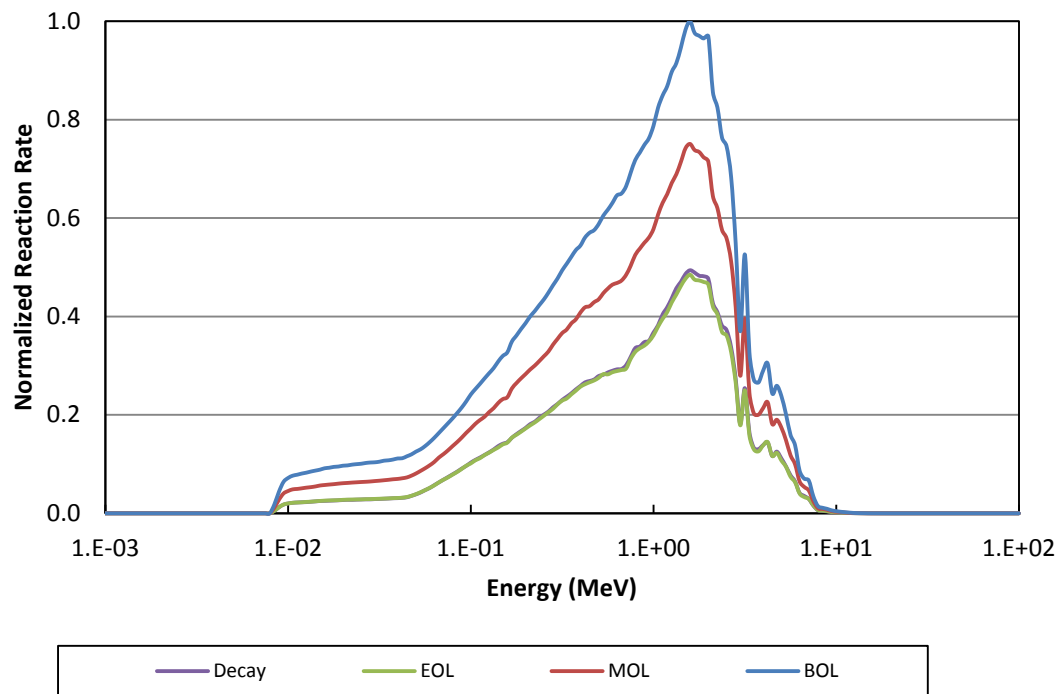


Figure IV-29 Inelastic scattering reaction rate of the core of the VHTR

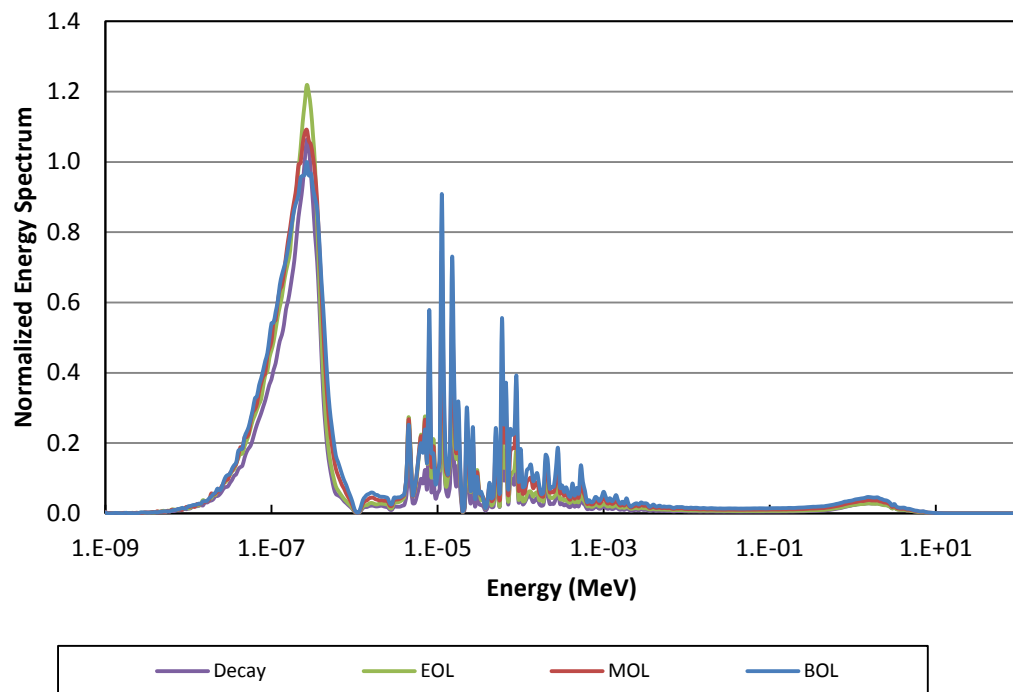


Figure IV-30 Energy deposition averaged over the core of the VHTR